

Metal–Organic Frameworks
How to cite: *Angew. Chem. Int. Ed.* **2021**, *60*, 11391–11397

International Edition: doi.org/10.1002/anie.202016882

German Edition: doi.org/10.1002/ange.202016882

High-Throughput Electron Diffraction Reveals a Hidden Novel Metal–Organic Framework for Electrocatalysis

Meng Ge⁺, Yanzhi Wang⁺, Francesco Carraro, Weibin Liang, Morteza Roostaenia, Samira Siahrostami, Davide M. Proserpio, Christian Doonan, Paolo Falcaro, Haoquan Zheng,^{*} Xiaodong Zou, and Zhehao Huang^{*}

Abstract: Metal-organic frameworks (MOFs) are known for their versatile combination of inorganic building units and organic linkers, which offers immense opportunities in a wide range of applications. However, many MOFs are typically synthesized as multiphase polycrystalline powders, which are challenging for studies by X-ray diffraction. Therefore, developing new structural characterization techniques is highly desired in order to accelerate discoveries of new materials. Here, we report a high-throughput approach for structural analysis of MOF nano- and sub-microcrystals by three-dimensional electron diffraction (3DED). A new zeolitic-imidazolate framework (ZIF), denoted ZIF-EC1, was first discovered in a trace amount during the study of a known ZIF-CO₃-1 material by 3DED. The structures of both ZIFs were solved and refined using 3DED data. ZIF-EC1 has a dense 3D framework structure, which is built by linking mono- and binuclear Zn clusters and 2-methylimidazoles (mIm⁻). With a composition of Zn₃(mIm)₅(OH), ZIF-EC1 exhibits high N and Zn densities. We show that the N-doped carbon material derived from ZIF-EC1 is a promising electrocatalyst for oxygen reduction reaction (ORR). The discovery of this new MOF and its conversion to an efficient electrocatalyst highlights the power of 3DED in developing new materials and their applications.

Introduction

Metal-organic frameworks (MOFs), or porous coordination polymers (PCPs), are a class of highly crystalline and porous hybrid materials constructed by linking metal clusters (or ions) and organic ligands via coordination bonds.^[1,2] In addition, their tunable structure metrics and topologies give rise to versatile properties,^[3] and vast opportunities for applications in gas storage,^[4,5] separation,^[6–9] catalysis,^[10–12] energy conversion and storage,^[13–19] and bio-medical science.^[20,21] With the access to almost unlimited combinations of inorganic building units and organic linkers, more than 80000 different MOFs have been reported over the past two decades.^[22] Interestingly, through the control of reaction kinetics or thermodynamics, different structures with distinct properties can be obtained even using the same building units.^[23–26] A relevant example is the large sub-class of MOFs termed zeolitic imidazolate frameworks (ZIFs),^[27] which are synthesized by connecting tetrahedrally-coordinated metal ions and linkers. These components can lead to a variety of topologies such as **sod**,^[28–30] **crb**,^[29] **dia**,^[30] **poz**,^[31] etc. Consequently, ZIFs with different topologies can commonly coexist in the bulk polycrystalline product. Accompanied by the tiny crystal sizes which are inaccessible to single crystal X-ray diffraction (SCXRD), structural characterization of these materials poses a major challenge, particularly when in search for new materials.

Powder X-ray diffraction (PXRD) is the most widely used technique for characterization of polycrystalline materials.

[*] M. Ge,^[†] X. Zou, Z. Huang
 Department of Materials and Environmental Chemistry, Stockholm University, 10691 Stockholm (Sweden)
 E-mail: zhehao.huang@mmk.su.se

Y. Wang,^[†] H. Zheng
 Key Laboratory of Applied Surface and Colloid Chemistry, Ministry of Education, School of Chemistry and Chemical Engineering, Shaanxi Normal University, Xi'an 710119 (China)
 E-mail: zhenghaoquan@snnu.edu.cn


F. Carraro, P. Falcaro
 Institute of Physical and Theoretical Chemistry, Graz University of Technology, Stremayrgasse 9, 8010 Graz (Austria)


W. Liang, C. Doonan
 Department of Chemistry and the Centre for Advanced Nanomaterials, The University of Adelaide
 Adelaide, 5005 South Australia (Australia)

M. Roostaenia, S. Siahrostami
 Department of Chemistry, University of Calgary
 2500 University Drive NW, Calgary, Alberta T2N1N4 (Canada)

D. M. Proserpio
 Dipartimento di Chimica, Università degli Studi di Milano
 20133 Milano (Italy)
 and
 Samara Center for Theoretical Materials Science (SCTMS), Samara State Technical University, Samara 443100 (Russia)

[†] These authors contributed equally to this work.

 Supporting information and the ORCID identification number(s) for the author(s) of this article can be found under <https://doi.org/10.1002/anie.202016882>.

 © 2021 The Authors. Angewandte Chemie International Edition published by Wiley-VCH GmbH. This is an open access article under the terms of the Creative Commons Attribution License, which permits use, distribution and reproduction in any medium, provided the original work is properly cited.

However, PXRD has a major drawback of peak overlapping, hindering accurate peak indexing and intensity extraction. This becomes more severe for samples containing several phases, which leads to either wrong phase assignments or no solution at all. Phase mixtures or polymorphs are often produced during the development of new materials. The aforementioned drawback of PXRD makes it especially challenging to study multiphasic materials containing new phases, which are likely to be overlooked, therefore preventing the discovery of new materials. Furthermore, the peak overlapping makes *ab initio* structure determination difficult and, in many cases, impossible. For MOFs, structural studies are even more difficult due to their relatively large unit cells that intensify the drawback of peak overlapping in PXRD patterns. These challenges are well tackled with the recent development of three-dimensional electron diffraction (3DED).^[32–34] Benefited from the strong interaction between electrons and matter, 3DED allows single crystal structural analysis even when the crystal sizes are down to the range of nanometers.^[35–39] This turns a polycrystalline powder into millions of analytes of single crystals. With a short data collection time of 3–5 minutes per crystal, it is therefore possible to analyze individual crystals in a high throughput manner and determine the structure of each tiny crystal in a phase mixture. More importantly, new materials in trace amounts can be discovered and their structures imparting unique properties can be revealed by 3DED.

Here, we report the first use of a 3DED technique, continuous rotation electron diffraction (cRED), in discovery of a new MOF among a phase mixture. The new MOF, denoted as ZIF-EC1 (EC: structure solved by Electron Crystallography), is constructed by linking Zn^{II} cations and deprotonated 2-methylimidazole (mIm[−]) linkers. It was discovered by cRED with a trace amount in a ZIF-CO₃-1 material. The atomic structures of both MOFs were successfully determined by cRED. Interestingly, the structure of ZIF-EC1 is rather dense, which is built by mono- and

binuclear Zn clusters. This offers a high density of N and Zn, which are active sites for electrocatalysis.^[40,41] Density functional theory (DFT) calculations show ZIF-EC1 has a higher stability than ZIF-CO₃-1. This provided insights for successfully obtaining a phase pure ZIF-EC1 material, which is important for catalysis. We subsequently converted pure ZIF-EC1 to N-doped carbon material as an electrocatalyst for oxygen reduction reaction (ORR). Due to the highly dense structure of ZIF-EC1, it leads to high contents of N and Zn in the derived carbon material. In addition, the oxygen atoms in the framework of ZIF-EC1 assist to generate a porous structure with high surface area, which is favorable for mass transfer. Owing to these advantages, the carbon material derived from ZIF-EC1 exhibits the best performance compared to those derived from other ZIFs including ZIF-1, ZIF-8, and ZIF-95. Our strategy by using cRED as a high throughput analytical tool would benefit communities beyond the MOF field to accelerate research in developing new materials.

Results and Discussion

PXRD is widely used to analyze polycrystalline products. Typically, structural analysis is done by matching peak positions in the experimental PXRD pattern with those calculated from possible structures in a crystallographic database, for example, the Cambridge Structure Database, which includes more than one million reported crystal structures.^[22] Nevertheless, this is often very challenging as shown in the case of the new ZIF-EC1 discovery. Using Zn^{II} cations and mIm[−] as the organic linker, we obtained a polycrystalline product, which shows a variation of particle sizes (0.2–5 μm) and morphologies (Figure S1). The PXRD pattern presents strong and sharp peaks, which indicates the sample has a good crystallinity (Figure 1 a). However, it was difficult to index the PXRD pattern, and the material was initially regarded as

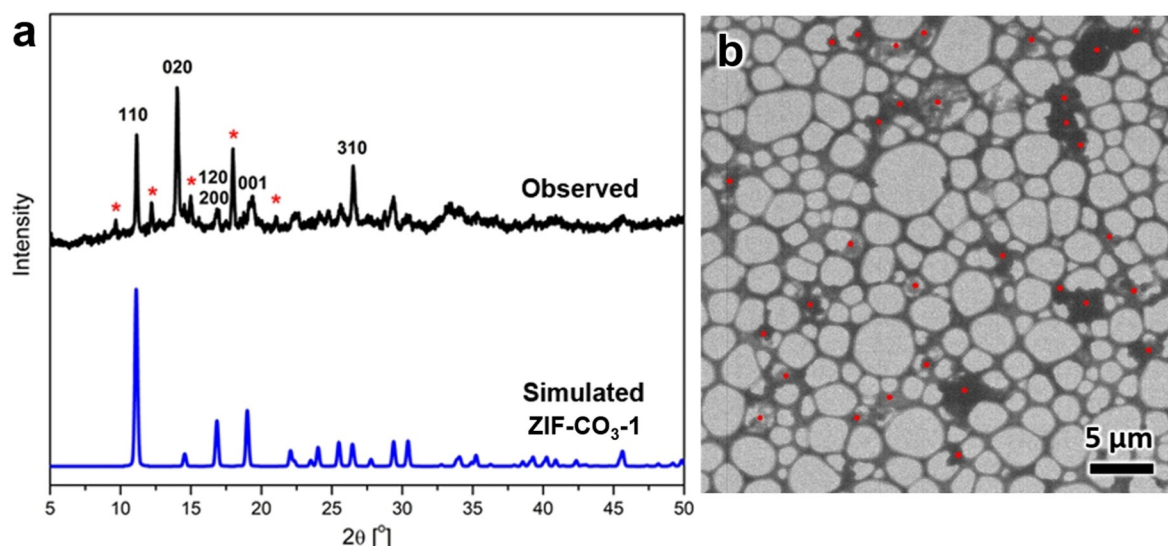


Figure 1. a) Comparison of observed PXRD pattern ($\lambda = 1.5406 \text{ \AA}$) with simulated pattern from the structural model of ZIF-CO₃-1. Many strong peaks (marked by asterisks) remain unidentified. b) TEM image showing individual nanocrystals (marked by red dots) in an area of $35 \times 35 \mu\text{m}^2$ studied by cRED.

a pure new phase (denoted as U14).^[42] Only after our investigations of ZIF-CO₃-1 by cRED,^[34] we could identify ZIF-CO₃-1 as the major phase in the sample (Figure 1 a). Yet, there are many peaks in the PXRD pattern that cannot be identified. As in most phase mixtures, the number of unindexed peaks belonging to a minor phase is too few that prevents phase identification and new structure determination.

3DED was applied to uniquely tackle these challenges on structural analysis of the new phase. It allows to identify and collect data from single nano- and sub-microcrystals. Remarkably, with the recent evolution of 3DED methods,^[43] data collection time has been reduced to a few minutes per crystal, providing a new strategy for high throughput phase analysis and crystal structure determination. As shown in the TEM image in Figure 1 b, more than 30 particles can be found and analyzed in an area of 35 × 35 μm². cRED data were collected from 11 individual nano- and sub-microcrystals with the rotation angles ranging from 39.26 to 117.45°, and the total data collection time of 1.5 to 4.3 min (Table S1, see Supporting Information for more details). By analyzing 3D reciprocal lattices reconstructed from the 11 cRED datasets, two distinct crystal systems and unit cells are revealed (Figure 2 and Figure S2). Nine crystals have an orthorhombic unit cell, with $a = 10.50 \text{ \AA}$, $b = 12.51 \text{ \AA}$, and $c = 4.69 \text{ \AA}$ and the remaining two exhibit a monoclinic unit cell, with $a = 13.58 \text{ \AA}$, $b = 14.55 \text{ \AA}$, $c = 14.31 \text{ \AA}$, and $\beta = 118.0^\circ$. The space group was deduced from the reflection conditions observed from the reconstructed reciprocal lattice, which is $Pba2$ (No. 32) or $Pbam$ (No. 55) for the former nine crystals and $P2_1/c$ (No. 14) for the latter two. The unit cell parameters and space group of the orthorhombic crystals agree to those of the ZIF-CO₃-1 phase as previously determined from pure samples.^[34,44] Meanwhile, no reported ZIFs match the unit cell and space group for the second phase, indicating it is a new MOF, which we denoted as ZIF-EC1.

Using the SHELX software package,^[45] ab initio structure determination was applied on each of the cRED datasets. The positions of all non-hydrogen atoms were found directly from the structure solution by direct methods. For the ZIF-CO₃-1 phase, the obtained structure is consistent with that determined by SCXRD (Figure S3). For the trace amount

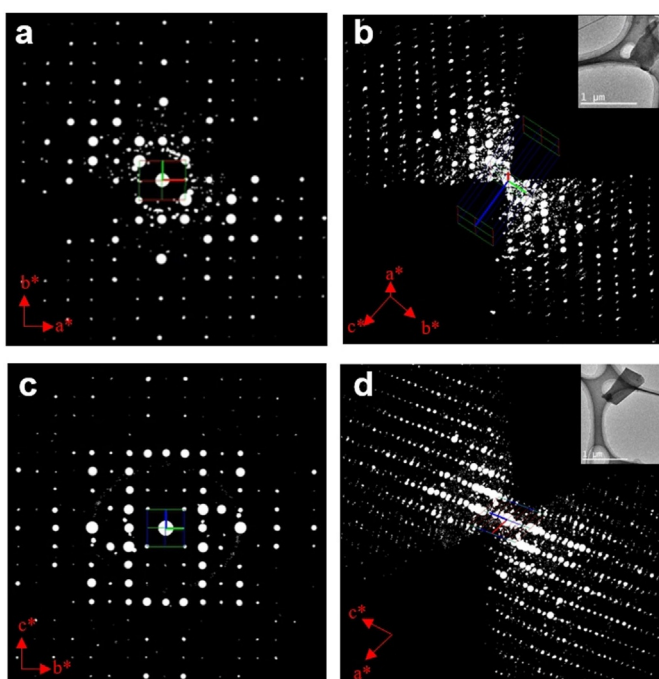


Figure 2. Reciprocal lattices reconstructed from cRED data. a,b) 2D slice showing the $hk0$ plane (a) cut from the 3D reciprocal lattice (b) of a ZIF-CO₃-1 crystal shown as the inset in (b). c,d) 2D slice showing the $0kl$ plane (c) cut from the 3D reciprocal lattice (d) of a ZIF-EC1 crystal shown as the inset in (d). Apart from the Bragg reflections, weak spots are attributed to the background noise. In addition, the amorphous carbon from the TEM grid and the bovine serum albumin (BSA) molecules used in the synthesis could also generate weak spots.

of the new ZIF-EC1 in the phase mixture, all three Zn^{II} cations and five mIm⁻ linkers in the asymmetric unit were located and the non-hydrogen atoms were refined anisotropically (see Table S2 for more details). ZIF-EC1 has a general formula of Zn₃(mIm)₅(OH). Each mIm⁻ linker connects to two Zn atoms. One of the three Zn cations is connected to four mIm⁻ linkers to form a ZnN₄ mononuclear cluster while the other two are coordinated to three mIm⁻ linkers and one bridging OH⁻ group to form a binuclear Zn₂N₆(OH) cluster (Figure 3 a). ZIF-EC1 is nonporous as shown in Figures 3 b

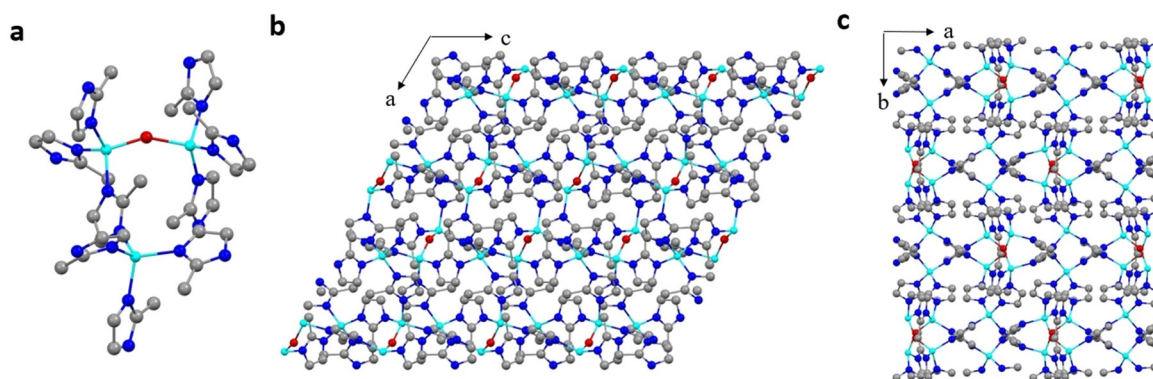


Figure 3. Structural model of ZIF-EC1. a) The coordination geometry of Zn. b,c) The framework structure viewing along b - and c -axis, respectively. Cyan spheres: Zn atoms; red spheres: O atoms; blue spheres: N atoms; grey spheres: C atoms. H atoms are not shown.

and c and S4. Topological analysis (Figure S5) of the ZIF-EC1 framework using ToposPro^[46] shows a rarely reported *γqt1* topology^[47–49] as found in the Samara Topological Data Center.^[50] PXRD patterns simulated from the structural models of ZIF-CO₃-1 and ZIF-EC1 are compared to the experimental PXRD pattern (Figure S6). All the peaks in the experimental PXRD pattern can finally be indexed by these two phases.

Despite the absence of porosity, ZIF-EC1 based on Zn mono- and binuclear clusters provides a higher density of metal and N sites as compared to ZIFs with only mononuclear Zn clusters (Table 1). The high density is favorable for catalysis. However, in order to study the properties and catalytic performance, a pure ZIF-EC1 material is highly desired. We therefore applied density functional theory (DFT) calculation to obtain the formation energy per atom and thus the stability of ZIF-CO₃-1 and ZIF-EC1. We used ZIF-8 as the reference since it has the lowest energy per atom (Figure 4b). These results indicate that ZIF-EC1 is thermodynamically more stable than ZIF-CO₃-1.

Nucleation rate plays an important role in MOF syntheses. Typically, the introduction of a competing reagent or modulator during the synthesis can inhibit and slow down the nucleation, which facilitates the formation of metastable crystalline products.^[53] Given that Zn(OAc)₂·2H₂O could react rapidly with HmIm to generate crystals at room temperature, the nucleation kinetics is crucial. To inhibit the formation of the metastable phase ZIF-CO₃-1 and promote the formation of the thermodynamically stable phase of ZIF-EC1, we used a synthetic condition that favors the nuclea-

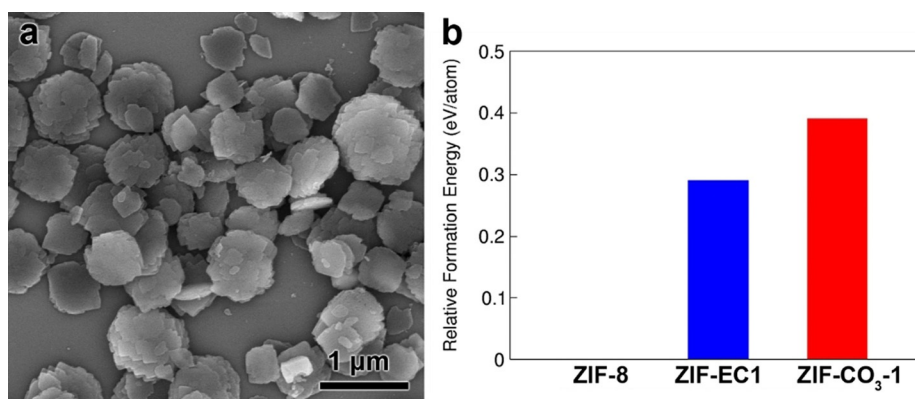


Figure 4. a) SEM image of pure ZIF-EC1 nanocrystals. b) Calculated relative formation energies using DFT calculations. The formation energies are calculated per atom for each ZIF structure. The formation energy of ZIF-8 is set to zero and the formation energy of ZIF-EC1 and ZIF-CO₃-1 are calculated relative to ZIF-8.

tion.^[54] Besides using an excess amount of HmIm (molar ratio HmIm/Zn = 16), the reaction of Zn(OAc)₂·2(H₂O) and HmIm was conducted under vigorous stirring to enhance the nucleation rate. Under this condition, a pure ZIF-EC1 sample was obtained. SEM images show that crystals of pure ZIF-EC1 have plate-like morphology (Figure 4a). Pawley fitting was applied to confirm the purity of the sample, which shows a good agreement between the observed and calculated patterns (Figure S7 and Table S3). In addition, ab initio structure determination was performed on the pure ZIF-EC1 phase, and the same crystal structure was obtained as that in the phase mixture (Figures S8, S9 and Table S2).

3DED provides a new strategy in searching for novel materials. Meanwhile, the structural insights obtained by 3DED reveal that the binuclear-based ZIF-EC1 could enhance catalytic performance through its high density of N and Zn. We therefore demonstrate ZIF-EC1 and its N-doped carbon derivative as electrocatalysts for ORR (Figures 5 and S10). SEM image shows that the morphology of nitrogen-doped carbon (NC) derived from ZIF-EC1 (denoted as NC-ZIF-EC1) after pyrolysis at 900 °C in Ar atmosphere remained the same as that of the pristine ZIF-EC1 (Figure S11). Applied as an electrocatalyst, NC-ZIF-EC1 exhibits an obvious oxygen reduction peak appearing at near 0.85 V in the cyclic voltammetry (CV) curve, confirming its electrocatalytic oxygen reduction activity (Figure 5a). The linear sweep voltammetry (LSV) shows that NC-ZIF-EC1 achieved promising onset potential ($E_{\text{onset}} = 0.930$ V) and half-wave potential ($E_{1/2} = 0.860$ V), which is comparable to that of Pt/C ($E_{1/2} = 0.867$, Figure 5b). Due to the Zn binuclear cluster, ZIF-EC1 has a high density

Table 1: Comparison of metal and nitrogen density of ZIF-EC1 to most reported ZIFs.

Name	Net	Composition	Density (Zn atoms nm ⁻³) ^[a]	Density (N atoms nm ⁻³) ^[a]	Reference
ZIF-EC1	<i>γqt1</i>	Zn ₃ (mIm) ₅ (OH)	4.77	15.90	This work
ZIF-1	crb	Zn(Im) ₂	3.64	14.56	[29]
ZIF-2	crb	Zn(Im) ₂	2.80	11.20	[29]
ZIF-3	dft	Zn(Im) ₂	2.66	10.64	[29]
ZIF-4	cag	Zn(Im) ₂	3.68	14.72	[29]
ZIF-6	gls	Zn(Im) ₂	2.31	9.24	[29]
ZIF-8	sod	Zn(mIm) ₂	2.47	9.88	[28, 29]
ZIF-10	mer	Zn(Im) ₂	2.25	9.00	[30]
ZIF-14	ana	Zn(eIm) ₂	2.57	10.28	[30, 51]
ZIF-22	lta	Zn(5abIm) ₂	2.02	8.08	[52]
ZIF-23	dia	Zn(4abIm) ₂	3.32	13.28	[52]
ZIF-71	rho	Zn(dclm) ₂	2.06	8.24	[30]
ZIF-77	frl	Zn(nIm)	3.22	12.88	[30]
ZIF-95	poz	Zn(cblm) ₂	1.51	6.04	[31]
ZIF-100	moz	Zn ₂₀ (mIm) ₃₉ (OH)	1.29	5.03	[31]

[a] See the Supporting Information for more details on calculating the density. Im = imidazolate; elm = 2-ethylimidazolate; 5abIm = 5-azabenzimidazolate; 4abIm = 4-azabenzimidazolate; dclm = 4,5-dicloroimidazolate; nIm = 2-nitroimidazolate; cblm = 5-chlorobenzimidazolate.

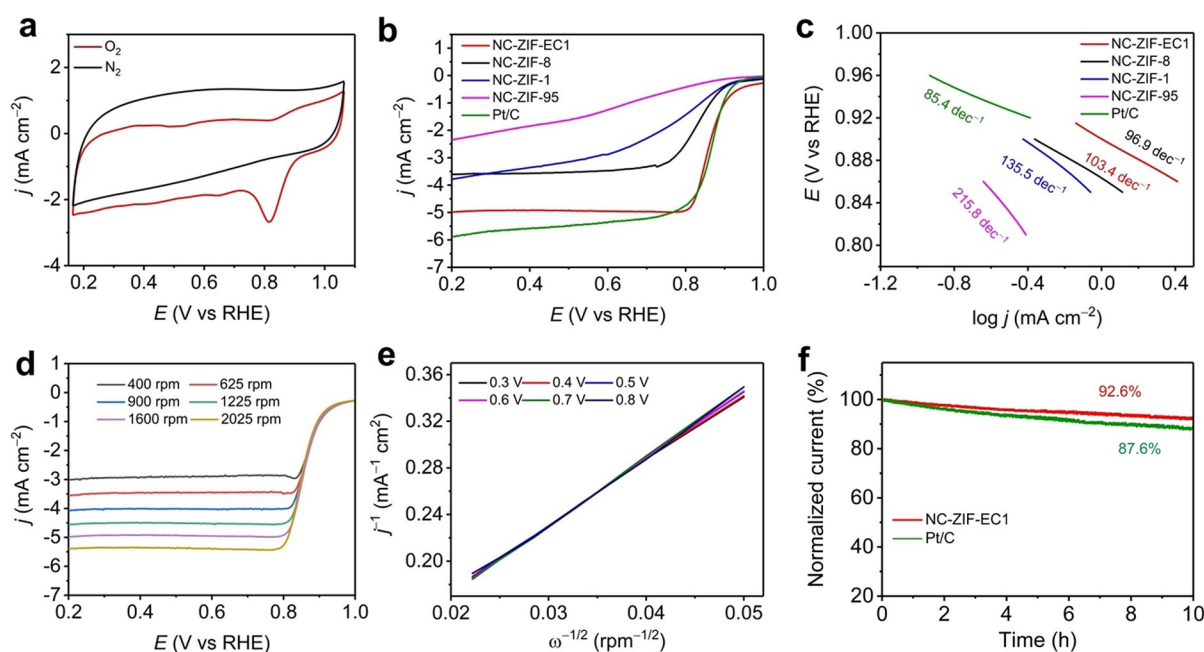


Figure 5. a) CV curves of NC-ZIF-EC1 in 0.1 M KOH solution saturated by N_2 and O_2 , respectively. b) LSV curves and c) Tafel plots of NC-ZIF-EC1, NC-ZIF-1, NC-ZIF-8, NC-ZIF-95, and Pt/C. d) LSV curves of NC-ZIF-EC1 at different rotating speeds. e) K - L plots at different potentials derived from data in (d). f) j - t chronoamperometric responses at 0.664 V (vs. RHE).

of N and Zn, which is 1.3–3.2 times higher than those in most reported low density ZIFs, such as ZIF-1, ZIF-8, and ZIF-95. Consequently, the weight percentages of N and Zn atoms, which serve as the active sites, are 2.1–4.3 times higher in NC-ZIF-EC1 than those in the nitrogen-doped carbons derived from ZIF-1, ZIF-8, and ZIF-95 (denoted as NC-ZIF-1, NC-ZIF-8, and NC-ZIF-95, respectively, Figures S12, S13, and Table S4). As a result, NC-ZIF-EC1 exhibits a better ORR activity than do the NC-ZIF-1, NC-ZIF-8, and NC-ZIF-95 (Figures 5b, S14–S17 and Table S5). In addition, ZIF-EC1 contains O atoms in the framework structure, which partially removes C atoms by evolution of CO/CO₂ during the pyrolysis.^[55,56] This not only reduces the carbon proportion in the NC-ZIF-EC1, but also facilitate the generation of large pores and high surface area (Figure S18), which contribute to the ORR activity by creating favorable mass transfer pathways. PXRD patterns of NCs show that all materials have partially graphitized structures (Figure S19a), while Raman spectra exhibit a similar amount of defective structure, indicating a similar graphitized structure among the NC materials (Figure S19b). By taking these advantages, in addition, NC-ZIF-EC1 outperforms most of the other state-of-the-art electrocatalysts, including MOFs,^[57,58] COFs,^[59,60] MOF derived carbon materials,^[61–64] carbon materials,^[41,65–67] and metal oxides,^[68,69] etc. (Table S6).

The electron transfer number (n) of NC-ZIF-EC1 was calculated to be ≈ 4.0 based on K - L plots, and ≈ 3.6 based on rotating ring disk electrode (RRDE) measurement (Figures 5d, e, and S20, see Supporting Information for more details). This indicates an outstanding $4e^-$ selectivity, which is a favorable reaction pathway to provide high reaction kinetics and prolong the durability of the cell. Combined with a higher density, which favors charge transfer during the electro-

catalysis, NC-ZIF-EC1 shows a better reaction kinetics as indicated by the lower Tafel slope compared to those in NC-ZIF-1, NC-ZIF-8, and NC-ZIF-95 (Figure 5c). The long-term durability of NC-ZIF-EC1 was evaluated using j - t chronoamperometric responses (Figure 5f). After 10 h, the current density of NC-ZIF-EC1 only dropped by 7.4%, which suggests a better stability compared to that of Pt/C. In addition, post-catalysis characterization shows that the morphology of NC-ZIF-EC1 remains intact after the ORR reactions (Figure S21).

Conclusion

By applying high throughput structural analysis on single nanocrystals of a phase mixture, we discovered a new MOF, ZIF-EC1. By controlling the reaction kinetics, pure ZIF-EC1 was synthesized. We present a proof-of-concept study that highlights the advantage of the 3DED technique in the development of MOF materials. Thanks to the new strategy, phases in trace amount and tiny crystals can be studied, which could accelerate the search for new MOFs. Revealing the structure uncovers the key property of ZIF-EC1, as it contains high density of metal sites and N atoms. As a result, the carbon material derived from ZIF-EC1 shows excellent electroactivity as compared to those of other Zn^{II} cation based ZIFs. We foresee that the application of 3DED technique will have a broad impact not only in the development of MOFs, but also in a wide range of materials and chemical compounds, such as metal oxides, polyoxometalates, and pharmaceutical compounds, where pure phases and large single crystals are difficult to obtain.

Deposition Number 2046826 contains the supplementary crystallographic data for this paper. These data are provided free of charge by the joint Cambridge Crystallographic Data Centre and Fachinformationszentrum Karlsruhe Access Structures service www.ccdc.cam.ac.uk/structures.

Acknowledgements

This research was supported by the Swedish Research Council (VR, 2016-04625, 2017-04321), the CATSS project from the Knut and Alice Wallenberg Foundation (KAW, 2016.0072), the National Natural Science Foundation of China (Grant No. 21975148, and 21601118), the Fundamental Research Funds for the Central Universities, and the Research Funds of Shaanxi Normal University. S.S. and M.R. acknowledge the support from the University of Calgary's Canada First Research Excellence Fund Program, the Global Research Initiative in Sustainable Low Carbon Unconventional Resources. F.C. and P.F. acknowledge European Union's Horizon 2020 Programme (FP/2014–2020)/ERC Grant Agreement no. 771834 POPCRYSTAL and TU Graz for the Lead Project (LP-03).

Conflict of interest

The authors declare no conflict of interest.

Keywords: continuous rotation electron diffraction · electrocatalysis · high throughput structural analysis · metal–organic frameworks · three-dimensional electron diffraction

- [1] O. M. Yaghi, G. Li, H. Li, *Nature* **1995**, *378*, 703–706.
- [2] S. Kitagawa, R. Kitaura, S. Noro, *Angew. Chem. Int. Ed.* **2004**, *43*, 2334–2375; *Angew. Chem.* **2004**, *116*, 2388–2430.
- [3] M. Eddaoudi, J. Kim, N. Rosi, D. Vodak, J. Wachter, M. O'Keeffe, O. M. Yaghi, *Science* **2002**, *295*, 469–472.
- [4] Q. Li, W. Zhang, O. Š. Miljanić, C.-H. Sue, Y.-L. Zhao, L. Liu, C. B. Knobler, J. F. Stoddart, O. M. Yaghi, *Science* **2009**, *325*, 855–859.
- [5] C. A. Trickett, A. Helal, B. A. Al-Maythaly, Z. H. Yamani, K. E. Cordova, O. M. Yaghi, *Nat. Rev. Mater.* **2017**, *2*, 17045.
- [6] J.-R. Li, J. Scully, H.-C. Zhou, *Chem. Rev.* **2012**, *112*, 869–932.
- [7] J. Duan, W. Jin, S. Kitagawa, *Coord. Chem. Rev.* **2017**, *332*, 48–74.
- [8] N. S. Bobbitt, M. L. Mendonca, A. J. Howarth, T. Islamoglu, J. T. Hupp, O. K. Farha, R. Q. Snurr, *Chem. Soc. Rev.* **2017**, *46*, 3357–3385.
- [9] R.-B. Lin, S. Xiang, H. Xing, W. Zhou, B. Chen, *Coord. Chem. Rev.* **2019**, *378*, 87–103.
- [10] J. Lee, O. K. Farha, J. Roberts, K. A. Scheidt, S. T. Nguyen, J. T. Hupp, *Chem. Soc. Rev.* **2009**, *38*, 1450–1459.
- [11] M. Yoon, R. Srirambalaji, K. Kim, *Chem. Rev.* **2012**, *112*, 1196–1231.
- [12] E. S. Gutterød, A. Lazzarini, T. Fjermestad, G. Kaur, M. Manzoli, S. Bordiga, S. Svelle, K. P. Lillerud, E. Skúlason, S. Øien-Ødegaard, A. Nova, U. Olsbye, *J. Am. Chem. Soc.* **2020**, *142*, 999–1009.
- [13] D. Sheberla, J. C. Bachman, J. S. Elias, C.-J. Sun, Y. Shao-Horn, M. Dincă, *Nat. Mater.* **2017**, *16*, 220–224.
- [14] D. Feng, T. Lei, M. R. Lukatskaya, J. Park, Z. Huang, M. Lee, L. Shaw, S. Chen, A. A. Yakovenko, A. Kulkarni, J. Xiao, K. Fredrickson, J. B. Tok, X. Zou, Y. Cui, Z. Bao, *Nat. Energy* **2018**, *3*, 30–36.
- [15] J. Park, M. Lee, D. Feng, Z. Huang, A. C. Hinckley, A. Yakovenko, X. Zou, Y. Cui, Z. Bao, *J. Am. Chem. Soc.* **2018**, *140*, 10315–10323.
- [16] S. Roy, Z. Huang, A. Bhunia, A. Castner, A. K. Gupta, X. Zou, S. Ott, *J. Am. Chem. Soc.* **2019**, *141*, 15942–15950.
- [17] K. W. Nam, S. S. Park, R. dos Reis, V. P. Dravid, H. Kim, C. A. Mirkin, J. F. Stoddart, *Nat. Commun.* **2019**, *10*, 4948.
- [18] C.-C. Hou, L. Zou, L. Sun, K. Zhang, Z. Liu, Y. Li, C. Li, R. Zou, J. Yu, Q. Xu, *Angew. Chem. Int. Ed.* **2020**, *59*, 7384–7389; *Angew. Chem.* **2020**, *132*, 7454–7459.
- [19] P. Deng, F. Yang, Z. Wang, S. Chen, Y. Zhou, S. Zaman, B. Y. Xia, *Angew. Chem. Int. Ed.* **2020**, *59*, 10807–10813; *Angew. Chem.* **2020**, *132*, 10899–10905.
- [20] P. Horcajada, R. Gref, T. Baati, P. K. Allan, G. Maurin, P. Couvreur, G. Férey, R. E. Morris, C. Serre, *Chem. Rev.* **2012**, *112*, 1232–1268.
- [21] C. Doonan, R. Riccò, K. Liang, D. Bradshaw, P. Falcaro, *Acc. Chem. Res.* **2017**, *50*, 1423–1432.
- [22] C. R. Groom, I. J. Bruno, M. P. Lightfoot, S. C. Ward, *Acta Crystallogr. Sect. B* **2016**, *72*, 171–179.
- [23] D. Feng, Z.-Y. Gu, J.-R. Li, H.-L. Jiang, Z. Wei, H.-C. Zhou, *Angew. Chem. Int. Ed.* **2012**, *51*, 10307–10310; *Angew. Chem.* **2012**, *124*, 10453–10456.
- [24] D. Feng, W.-C. Chung, Z. Wei, Z.-Y. Gu, H.-L. Jiang, Y.-P. Chen, D. J. Darensbourg, H.-C. Zhou, *J. Am. Chem. Soc.* **2013**, *135*, 17105–17110.
- [25] T. He, Z. Huang, S. Yuan, X.-L. Lv, X.-J. Kong, X. Zou, H.-C. Zhou, J.-R. Li, *J. Am. Chem. Soc.* **2020**, *142*, 13491–13499.
- [26] M. O. Cichocka, Z. Liang, D. Feng, S. Back, S. Siahrostami, X. Wang, L. Samperisi, Y. Sun, H. Xu, N. Hedin, H. Zheng, X. Zou, H.-C. Zhou, Z. Huang, *J. Am. Chem. Soc.* **2020**, *142*, 15386–15395.
- [27] A. Phan, C. J. Doonan, F. J. Uribe-Romo, C. B. Knobler, M. O'Keeffe, O. M. Yaghi, *Acc. Chem. Res.* **2010**, *43*, 58–67.
- [28] X. Huang, J. Zhang, X. Chen, *Chin. Sci. Bull.* **2003**, *48*, 1531–1534.
- [29] K. S. Park, Z. Ni, A. P. Côté, J. Y. Choi, R. Huang, F. J. Uribe-Romo, H. K. Chae, M. O'Keeffe, O. M. Yaghi, *Proc. Natl. Acad. Sci. USA* **2006**, *103*, 10186–10191.
- [30] R. Banerjee, A. Phan, B. Wang, C. Knobler, H. Furukawa, M. O'Keeffe, O. M. Yaghi, *Science* **2008**, *319*, 939–943.
- [31] B. Wang, A. P. Côté, H. Furukawa, M. O'Keeffe, O. M. Yaghi, *Nature* **2008**, *453*, 207–211.
- [32] W. Wan, J. Sun, J. Su, S. Hovmöller, X. Zou, *J. Appl. Crystallogr.* **2013**, *46*, 1863–1873.
- [33] B. L. Nannenga, D. Shi, A. G. W. Leslie, T. Gonen, *Nat. Methods* **2014**, *11*, 927–930.
- [34] Z. Huang, M. Ge, F. Carraro, C. Doonan, P. Falcaro, X. Zou, *Faraday Discuss.* **2021**, *225*, 118–132.
- [35] M. Gemmi, E. Mugnaioli, T. E. Gorelik, U. Kolb, L. Palatinus, P. Boullay, S. Hovmöller, J. P. Abrahams, *ACS Cent. Sci.* **2019**, *5*, 1315–1329.
- [36] S. Yuan, J.-S. Qin, H.-Q. Xu, J. Su, D. Rossi, Y. Chen, L. Zhang, C. Lollar, Q. Wang, H.-L. Jiang, D. H. Son, H. Xu, Z. Huang, X. Zou, H.-C. Zhou, *ACS Cent. Sci.* **2018**, *4*, 105–111.
- [37] J. Li, C. Lin, Y. Min, Y. Yuan, G. Li, S. Yang, P. Manuel, J. Lin, J. Sun, *J. Am. Chem. Soc.* **2019**, *141*, 4990–4996.
- [38] Z. Huang, E. S. Grape, J. Li, A. K. Inge, X. Zou, *Coord. Chem. Rev.* **2021**, *427*, 213583.
- [39] Z. Huang, T. Willhammar, X. Zou, *Chem. Sci.* **2021**, *12*, 1206–1219.
- [40] D. Guo, R. Shibuya, C. Akiba, S. Saji, T. Kondo, J. Nakamura, *Science* **2016**, *351*, 361–365.

- [41] J. Li, S. Chen, N. Yang, M. Deng, S. Ibraheem, J. Deng, J. Li, L. Li, Z. Wei, *Angew. Chem. Int. Ed.* **2019**, *58*, 7035–7039; *Angew. Chem.* **2019**, *131*, 7109–7113.
- [42] F. Carraro, M. de J. Velásquez-Hernández, E. Astria, W. Liang, L. Twhight, C. Parise, M. Ge, Z. Huang, R. Ricco, X. Zou, L. Villanova, C. O. Kappe, C. Doonan, P. Falcaro, *Chem. Sci.* **2020**, *11*, 3397–3404.
- [43] M. O. Cichocka, J. Ångström, B. Wang, X. Zou, S. Smeets, *J. Appl. Crystallogr.* **2018**, *51*, 1652–1661.
- [44] S. A. Basnayake, J. Su, X. Zou, K. J. Balkus, *Inorg. Chem.* **2015**, *54*, 1816–1821.
- [45] G. M. Sheldrick, *Acta Crystallogr. Sect. A* **2008**, *64*, 112–122.
- [46] V. A. Blatov, A. P. Shevchenko, D. M. Proserpio, *Cryst. Growth Des.* **2014**, *14*, 3576–3586.
- [47] S.-Y. Yao, Y.-Q. Tian, *CrystEngComm* **2010**, *12*, 697–699.
- [48] Y.-Q. Tian, S.-Y. Yao, D. Gu, K.-H. Cui, D.-W. Guo, G. Zhang, Z.-X. Chen, D.-Y. Zhao, *Chem. Eur. J.* **2010**, *16*, 1137–1141.
- [49] S. Glante, S. Bette, G. Gallo, R. E. Dinnebier, M. Hartmann, *Cryst. Growth Des.* **2019**, *19*, 4844–4853.
- [50] see: <https://topcryst.com/>.
- [51] X.-C. Huang, Y.-Y. Lin, J.-P. Zhang, X.-M. Chen, *Angew. Chem. Int. Ed.* **2006**, *45*, 1557–1559; *Angew. Chem.* **2006**, *118*, 1587–1589.
- [52] H. Hayashi, A. P. Côté, H. Furukawa, M. O’Keeffe, O. M. Yaghi, *Nat. Mater.* **2007**, *6*, 501–506.
- [53] A. Schaate, P. Roy, A. Godt, J. Lippke, F. Waltz, M. Wiebcke, P. Behrens, *Chem. Eur. J.* **2011**, *17*, 6643–6651.
- [54] W. Liang, R. Ricco, N. K. Maddigan, R. P. Dickinson, H. Xu, Q. Li, C. J. Sumby, S. G. Bell, P. Falcaro, C. J. Doonan, *Chem. Mater.* **2018**, *30*, 1069–1077.
- [55] L. Ye, Y. Ying, D. Sun, Z. Zhang, L. Fei, Z. Wen, J. Qiao, H. Huang, *Angew. Chem. Int. Ed.* **2020**, *59*, 3244–3251; *Angew. Chem.* **2020**, *132*, 3270–3277.
- [56] L. Ye, G. Chai, Z. Wen, *Adv. Funct. Mater.* **2017**, *27*, 1606190.
- [57] E. M. Miner, T. Fukushima, D. Sheberla, L. Sun, Y. Surendranath, M. Dincă, *Nat. Commun.* **2016**, *7*, 10942.
- [58] H. Zhong, K. H. Ly, M. Wang, Y. Krupskaya, X. Han, J. Zhang, J. Zhang, V. Kataev, B. Büchner, I. M. Weidinger, S. Kaskel, P. Liu, M. Chen, R. Dong, X. Feng, *Angew. Chem. Int. Ed.* **2019**, *58*, 10677–10682; *Angew. Chem.* **2019**, *131*, 10787–10792.
- [59] N. Zion, D. A. Cullen, P. Zelenay, L. Elbaz, *Angew. Chem. Int. Ed.* **2020**, *59*, 2483–2489; *Angew. Chem.* **2020**, *132*, 2504–2510.
- [60] S. Yang, Y. Yu, M. Dou, Z. Zhang, L. Dai, F. Wang, *Angew. Chem. Int. Ed.* **2019**, *58*, 14724–14730; *Angew. Chem.* **2019**, *131*, 14866–14872.
- [61] J. Wang, W. Zang, S. Xi, M. Kosari, S. J. Pennycook, H. C. Zeng, *J. Mater. Chem. A* **2020**, *8*, 17266–17275.
- [62] C. Liu, J. Wang, J. Li, J. Liu, C. Wang, X. Sun, J. Shen, W. Han, L. Wang, *J. Mater. Chem. A* **2017**, *5*, 1211–1220.
- [63] L. Zou, C.-C. Hou, Z. Liu, H. Pang, Q. Xu, *J. Am. Chem. Soc.* **2018**, *140*, 15393–15401.
- [64] X. F. Lu, Y. Chen, S. Wang, S. Gao, X. W. (David) Lou, *Adv. Mater.* **2019**, *31*, 1902339.
- [65] J. Wang, H. Li, S. Liu, Y. Hu, J. Zhang, M. Xia, Y. Hou, J. Tse, J. Zhang, Y. Zhao, *Angew. Chem. Int. Ed.* **2021**, *60*, 181–185; *Angew. Chem.* **2021**, *133*, 183–187.
- [66] P. Song, M. Luo, X. Liu, W. Xing, W. Xu, Z. Jiang, L. Gu, *Adv. Funct. Mater.* **2017**, *27*, 1700802.
- [67] B. Chen, X. He, F. Yin, H. Wang, D.-J. Liu, R. Shi, J. Chen, H. Yin, *Adv. Funct. Mater.* **2017**, *27*, 1700795.
- [68] L.-H. Xu, H.-B. Zeng, X.-J. Zhang, S. Cosnier, R. S. Marks, D. Shan, *J. Catal.* **2019**, *377*, 20–27.
- [69] C. Mu, J. Mao, J. Guo, Q. Guo, Z. Li, W. Qin, Z. Hu, K. Davey, T. Ling, S.-Z. Qiao, *Adv. Mater.* **2020**, *32*, 1907168.

Manuscript received: December 21, 2020

Accepted manuscript online: March 7, 2021

Version of record online: April 7, 2021

Supporting Information

High-Throughput Electron Diffraction Reveals a Hidden Novel Metal–Organic Framework for Electrocatalysis

Meng Ge⁺, Yanzhi Wang⁺, Francesco Carraro, Weibin Liang, Morteza Roostaenia, Samira Siahrostami, Davide M. Proserpio, Christian Doonan, Paolo Falcaro, Haoquan Zheng, Xiaodong Zou, and Zhehao Huang**

anie_202016882_sm_miscellaneous_information.pdf

Table of Contents:

Section 1. Materials and instrumentation

Section 2. Synthesis of ZIF-EC1

Section 3. Structural analysis by cRED

Section 4. Energy calculation of ZIF-EC1

Section 5. Electrochemical analysis of ZIF-EC1 and its derivatives

Section 1. Materials and instrumentation

Materials.

Zn(NO₃)₂·6H₂O (99.9%), Zn(OAc)₂·2H₂O (99.9%), 2-methylimidazole (HmIm) (99%), Imidazole (HIm) (99%), 5-chlorobenzimidazole (HcbIm) (97%) were purchased from the Energy Chemical. Ethanol (AR, 99.5%), Methanol (AR, 99.5%), N,N-Dimethylformamide (AR, 99.5%), Dichloromethane (AR, 99.5%) were purchased from Sinopharm Chemical Reagent Co. All the reagents were used without further purification unless otherwise mentioned. Deionized water was used throughout the experimental processes.

Methods.

Scanning electron microscopy (SEM). SEM images were performed on a JEOL JSM-7000F scanning electron microscope with a field emission gun capable of generating and collecting high-resolution and low-vacuum images. The field emission gun assembles with a Schottky emitter source. The images were obtained at an accelerating voltage of 15.0 kV, with beam current of 200 μA.

Powder X-ray diffraction (PXRD). PXRD patterns were recorded on a PANalytical X'Pert Pro diffractometer equipped with a Pixel detector and a monochromator, using Cu K_{α1} radiation ($\lambda = 1.5406 \text{ \AA}$). Data was recorded using a current of 40 mA, accelerating voltage of 40 V and source silt 15 mm.

Electrochemical evaluation. All electrochemical tests were carried out on CHI 660E electrochemical workstation at 30 °C. Oxygen reduction reaction (ORR) performances were evaluated by a three-electrode system. The working electrode was a rotating disk electrode (RDE) with a diameter of 5 mm (0.196 cm²). The counter electrode was a graphite rod and the reference electrode was a saturated Ag/AgCl electrode. The cyclic voltammetry (CV) test was carried out in 0.1 M KOH saturated with O₂ (scan rate is 50 mV s⁻¹). The linear sweep voltammetry (LSV) test was carried out in 0.1 M KOH saturated with O₂, and the speed range was 400 to 2025 rpm (scan rate was 5 mV s⁻¹). Current-time chronoamperometric responses were measured at 0.66 V (relative to RHE). The catalyst ink for ORR tests was prepared as the following: 4 mg catalyst was dispersed in a mixed solution containing 660 μL isopropanol, 330 μL deionized water and 10 μL Nafion aqueous solution (5 wt%). The mixed solution was treated by ultrasound for 1 h to form a homogeneous suspension. Then 20 μL catalyst solution was taken from the pipette and uniformly dripped onto the rotating disc electrode (RDE) (catalyst loading was about 0.4 mg cm⁻²). After natural drying, a homogeneous film was formed.

Section 2. Synthesis of ZIF-EC1

Synthesis of ZIF-EC1 and ZIF-CO₃-1 mixture. In a typical synthesis, 300 μL of a 440 mM aqueous solution of HmIM, 60 μL of a 36 mg mL⁻¹ aqueous solution of bovine serum albumin (BSA) and 1140 μL of deionized water were mixed in a 2 ml plastic centrifuge tube for 1 minute. Then, the solution was added to 500 μL of an 80 mM aqueous solution of Zn(OAc)₂·2(H₂O). The

mixture was left under static conditions at RT for 24 h. White powder was then harvested by centrifugation followed by washing by deionized water for at least six times.

Synthesis of pure ZIF-EC1. In a typical synthesis of pure ZIF-EC1, 0.125 mL of a 3.84 M aqueous solution of HmIM was mixed with 1.875 mL of deionized water. 1 mL of 0.24 M aqueous solution of $\text{Zn}(\text{OAc})_2 \cdot 2(\text{H}_2\text{O})$ was added into the above solution under vigorous stirring condition. The mixture was kept under stirring at RT for at least 4 h. White powder was then harvested by centrifugation followed by washing by deionized water for at least six times.

Synthesis of ZIF-8. In a typical synthesis of pure ZIF-8, 100 mg HmIm was dissolved in 10 mL of methanol to form solution A. 140 mg $\text{Zn}(\text{NO}_3)_2 \cdot 6\text{H}_2\text{O}$ was dissolved in another 10 mL methanol to form solution B. Then, solution B was poured into solution A under magnetic stirring for 10 min and aged for 24 h at room temperature. The product was collected by centrifugation and washed with methanol. It was then dried overnight in a freeze dryer for characterization.

Synthesis of ZIF-1. In a typical synthesis of pure ZIF-1, 100 mg $\text{Zn}(\text{NO}_3)_2 \cdot 6\text{H}_2\text{O}$ and 150 mg HIm are dissolved in a glass bottle containing 18 mL DMF. After vigorous stirring, the vial was capped and heated in a thermostat at 85 °C for 24 h. After the reaction is completed, it is naturally cooled to room temperature. The product was collected by centrifugation and washed with dichloromethane. It was then dried overnight in a freeze dryer for characterization.

Synthesis of ZIF-95. In a typical synthesis of pure ZIF-95, 237.5 mg $\text{Zn}(\text{NO}_3)_2 \cdot 6\text{H}_2\text{O}$ and 1221 mg HcbIm were added to a beaker containing 55 ml DMF and 5 ml water. After stirring for 2 h, the mixed solution was added to a stainless steel autoclave lined with Teflon, and then heated in an air circulating oven at 120 °C for 3 days. The product was collected by centrifugation, washed with methanol and DMF, and then dried overnight in a freeze dryer for characterization.

Synthesis of N doped carbon from ZIF materials. The as-prepared ZIF-EC1, ZIF-1, ZIF-8 and ZIF-95 materials were annealed at 900 °C for 2 h at a ramp rate of 5 °C min⁻¹ in flowing Ar in a tube furnace. Finally, the N doped carbon electrocatalysts were obtained.

Section 3. Structural analysis by cRED

The samples for high throughput cRED investigations were crushed in a mortar and dispersed in deionized water. A droplet was then taken from the suspension, transferred to a copper grid covered with lacey carbon, and dried in air at room temperature. cRED data were collected on a JEOL JEM2100 microscope operated at 200 kV (Cs 1.0 mm, point resolution 0.23 nm). TEM images were recorded with a Gatan Orius 833 CCD camera (resolution 2048 x 2048 pixels, pixel size 7.4 μm). cRED data collection was controlled by using the data acquisition software *Instamatic*^[1], and electron diffraction (ED) frames were recorded with a Timepix hybrid detector QTPX-262k (512 x 512 pixels, pixel size 55 μm, max 120 frames/second, Amsterdam Sci. Ins.). A single-tilt holder was used for the data collection, which could tilt from -60° to +60° in the TEM. The area used for cRED data collection was about 1.0 μm in diameter, defined using a selected-area aperture. To minimize electron beam damage on the crystals, a low electron dose and high

rotation speed were applied. The high throughput cRED method can benefit for virtualization and identification of each individual nanocrystals. As shown in Figure 1b, ~30 nanocrystals can be analyzed in an area of $35 \times 35 \mu\text{m}^2$. By taking advantage of continuous rotation, it takes less than 5 minutes to collect a complete cRED dataset. For ZIF-CO₃-1, a typical cRED dataset covered a crystal rotation angle of 100.2° and took 3.7 min to collect. For ZIF-EC1, the rotation range was 117.5° and the collection time was 4.3 min.

The obtained cRED data were analyzed by using *REDprocessing* software package^[2]. Two sets of unit cells and space groups were determined from 11 nanocrystals in phase mixture, indicating it contains two different structures. For the major phase, one typical unit cell was determined as $a = 10.57 \text{ \AA}$, $b = 12.40 \text{ \AA}$, $c = 4.65 \text{ \AA}$, $\alpha = 90.8^\circ$, $\beta = 90.9^\circ$, and $\gamma = 91.6^\circ$. The intensity distribution of reflections in the 3D reciprocal lattice indicates that the crystal is orthorhombic with a Laue class of *mmm* (Figures S2a-d). The unit cell angles α , β , and γ are near 90° , which also confirms the orthorhombic crystal system. The reflection conditions were deduced from the 2D slice cuts as $0kl: k = 2n$; $h0l: h = 2n$; $h00, h = 2n$; $0k0: k = 2n$, which corresponds to two possible space groups of *Pba2* (No. 32), and *Pbam* (No. 55). For the minor phase, the unit cell parameters were determined to be $a = 13.65 \text{ \AA}$, $b = 14.36 \text{ \AA}$, $c = 14.30 \text{ \AA}$, $\alpha = 90.3^\circ$, $\beta = 117.5^\circ$, and $\gamma = 90.6^\circ$. The intensity distribution of reflections in the 3D reciprocal lattice indicates that the crystal is monoclinic with a Laue class of *2/m* (Figures S2e-f). The reflection conditions was deduced as $0k0: k=2n$; $00l: l=2n$; $h0l: l=2n$, which corresponds to the space group: *P2₁/c* (No. 14). The details of data collection and unit cell determination are summarized in Table S1.

After changing the synthetic conditions, we applied the high throughput cRED method on the product obtained using the optimized synthesis condition for ZIF-EC1. The sample purity was further confirmed by Pawley fitting of the PXRD pattern (Figure S6). With improved crystallinity, cRED dataset with higher resolution and higher completeness were obtained (Figure S7). The intensities of the reflections were extracted from the cRED data using the X-ray Detector Software (*XDS*)^[3]. To obtain a high data completeness, nine cRED datasets were merged to a resolution of 0.78 \AA and a completeness of 89.5% using *XSCALE*. Structure solution and refinement were conducted by using the SHELX software package⁵. In the refinement of the merged dataset, distance (DFIX) and planarity (FLAT) restraints were applied to the 2-methylimidazolate linkers to maintain a reasonable geometry. EADP was applied on two carbon atoms on the imidazolate group. In addition, EXTI was used in the final refinement, which converged with the agreement values $R_1=0.1811$ for $4103 F_o > 4\sigma(F_o)$ and 0.1984 for all 5116 data for 302 parameters (Table S2).

After knowing the structure of ZIF-EC1, we calculated its metal and nitrogen density and compared them to most reported ZIFs (Table 1). The metal density was calculated as

$$\text{metal density} = \frac{\text{number of metal atoms per unit cell}}{\text{unit cell volume}}$$

where the number of metal atoms per unit cell and the unit cell volume are read from the cif file. For example, the Zn atom density in ZIF-EC1 was calculated as

$$\frac{12}{2514.7 \text{ \AA}^3} = 4.77 \text{ nm}^{-3}$$

The nitrogen density is calculated in a similar way as

$$\text{nitrogen density} = \frac{\text{number of nitrogen atoms per unit cell}}{\text{unit cell volume}}$$

For example, the N atom density in ZIF-EC1 was calculated as

$$\frac{40}{2514.7 \text{ \AA}^3} = 15.90 \text{ nm}^{-3}$$

Section 4. Energy calculation of ZIF-EC1

Atomic Simulation Environment (ASE)^[4] was used to handle the simulation and the QUANTUM ESPRESSO program package^[5] to perform electronic structure calculations. The electronic wavefunctions were expanded in plane waves up to a cutoff energy of 800 eV, while the electron density is represented on a grid with an energy cutoff of 8000 eV after carrying out the convergence tests. Core electrons were approximated using ultrasoft pseudopotentials^[6]. The ground state energies of ZIF-EC1, ZIF-CO₃-1 and ZIF-8 bulk structures were calculated using PBE exchange-correlation functional with dispersion correction^[7]. The Brillouin zone were converged and sampled with (3 × 3 × 3) Monkhorst-Pack k-points.

Section 5. Electrochemical analysis of ZIF-EC1 and its derivatives

The potentials corresponding to the reversible hydrogen electrode (RHE) electrode were calculated with the following equation:

$$E_{RHE} = E_{Ag/AgCl} + (0.197 + 0.0591 \times \text{pH}) \quad \text{Eq (1)}$$

The electron transfer numbers (n) were calculated with Koutecky-Levich (K-L) equation:

$$1/j = 1/j_l + 1/j_k = 1/B\omega^{1/2} + 1/j_k \quad \text{Eq (2)}$$

where j is the measured current density; j_l is the diffusion current density; j_k is the kinetic current density; ω is the rotation speed in rpm; B can be confirmed by Koutecky-Levich (K-L) equation:

$$B = 0.2nFC_0(D_0)^{2/3}/\nu^{-1/6} \quad \text{Eq (3)}$$

where n is the transfer number; F is the Faraday constant (96485 C mol⁻¹); C_0 is the concentration of O₂ in 0.1 M KOH (1.2×10⁻⁶ mol cm⁻³); D_0 is the diffusion coefficient of O₂ in 0.1 M KOH (1.9×10⁻⁵ cm² s⁻¹); ν is the viscosity of 0.1 M KOH (0.1 cm² s⁻¹). The transfer number (n) was obtained by using the equations.

The LSV curve of ZIF-EC1 in 0.1 M KOH solution saturated by O₂ is shown in Figure S9. The E_{1/2} of ZIF-EC1 was measured to be 0.757 V, indicating a moderate ORR activity. The high density of surface Zn-N_x structure could attribute to the good ORR activity. However, MOF materials are limited by their conductivities when being used as electrocatalysts for ORR. ZIF-EC1 possesses a high density of activity sites. NC-ZIF-EC1 derived from ZIF-EC1 has the highest N loading compared to those of NC-ZIF-1, NC-ZIF-8, and NC-ZIF-95 (Figures S15, S16 and Table S4). The I_D/I_G of NC-ZIF-EC1, NC-ZIF-1, NC-ZIF-8, and NC-ZIF-95 is 1.08, 1.35, 1.04, 1.08, respectively (Figure S17). PXRD shows that all samples exhibit two similar broad peaks assigned to partial graphitized carbon. The results shown in Figure 5 indicates that NC-ZIF-EC1 exhibits the best ORR activity among all carbon based materials derived from ZIFs, which is also compatible to that of commercial Pt/C. A Tafel slope of 96.9 mV dec⁻¹ is observed for NC-ZIF-EC1, which is considerably lower than that of NC-ZIF-1 (135.5 mV dec⁻¹), NC-ZIF-8 (103.4 mV dec⁻¹), and NC-ZIF-95 (215.8 mV dec⁻¹) (Figure 5c). This indicates a favorable reaction kinetics for NC-ZIF-EC1 compared to NC-ZIF-1, NC-ZIF-8, and NC-ZIF-95.

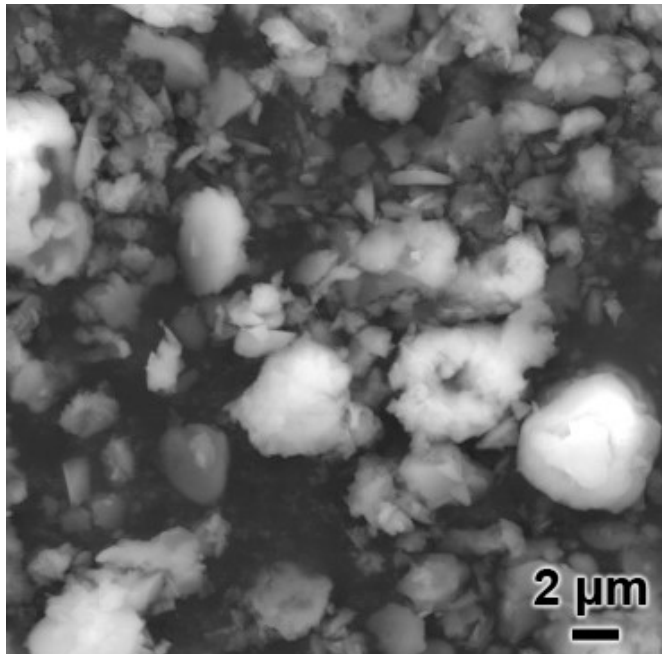


Figure S1. SEM image of the obtained product, showing a variation of particle sizes and morphologies.

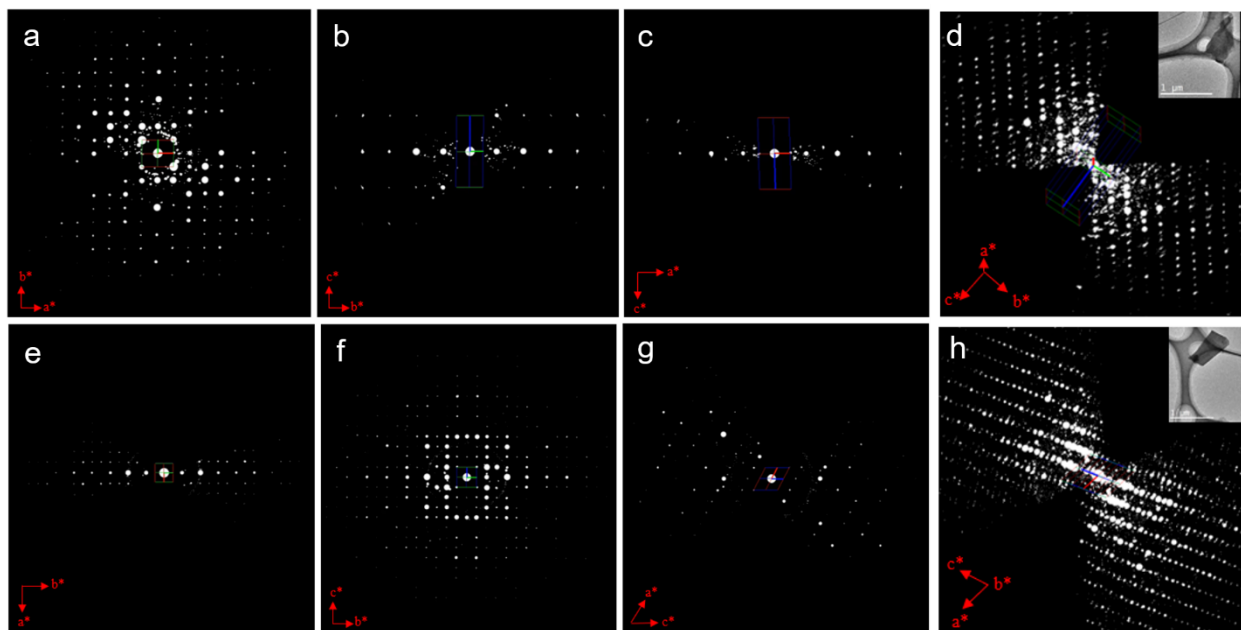


Figure S2. (a-c) 2D slice cuts from the reconstructed 3D reciprocal lattice of ZIF-CO₃-1 showing the (a) $hk0$, (b) $0kl$, and (c) $h0l$ planes. (d) 3D reciprocal lattice of ZIF-CO₃-1. (e-g) 2D slice cuts from the reconstructed 3D reciprocal lattice of ZIF-EC1 showing the (e) $hk0$, (f) $0kl$, and (g) $h0l$ planes. (h) 3D reciprocal lattice of ZIF-EC1.

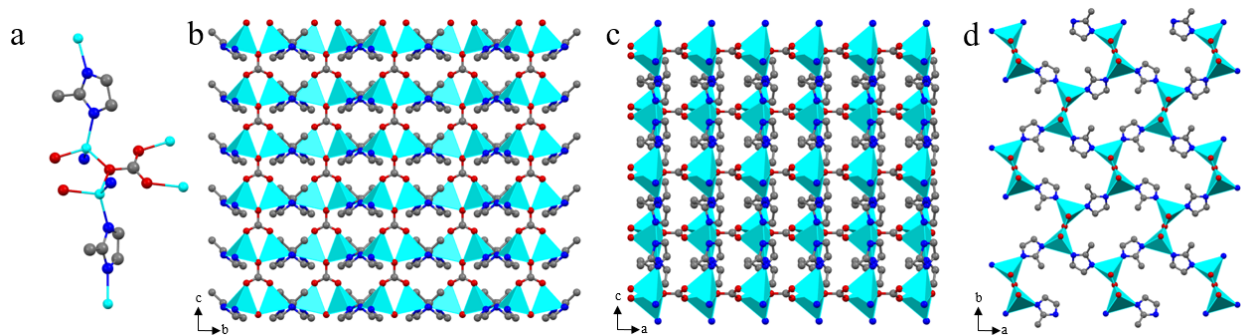


Figure S3. Structural model of ZIF-CO₃-1. (a) The coordination geometry of Zn. (b-d) The framework structure viewing along a -, b - and c -axis, respectively. Cyan tetrahedra: Zn atoms; red spheres: O atoms; blue spheres: N atoms; grey spheres: C atoms.

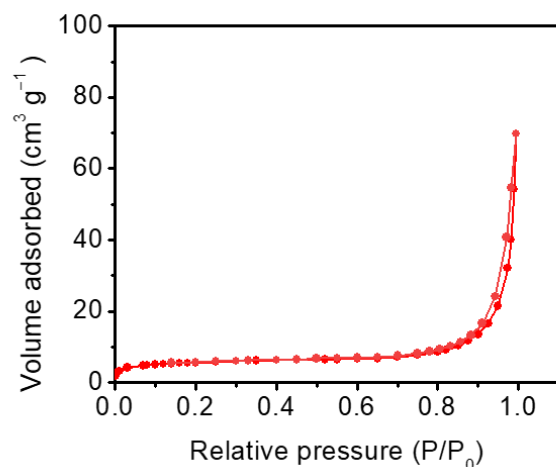


Figure S4. N₂ adsorption-desorption isotherm of ZIF-EC1. ZIF-EC1 is nonporous to N₂. The porosity showed in the P/P₀ range > 0.9 is caused by interparticle voids. The BET surface area is 19.7 m² g⁻¹.

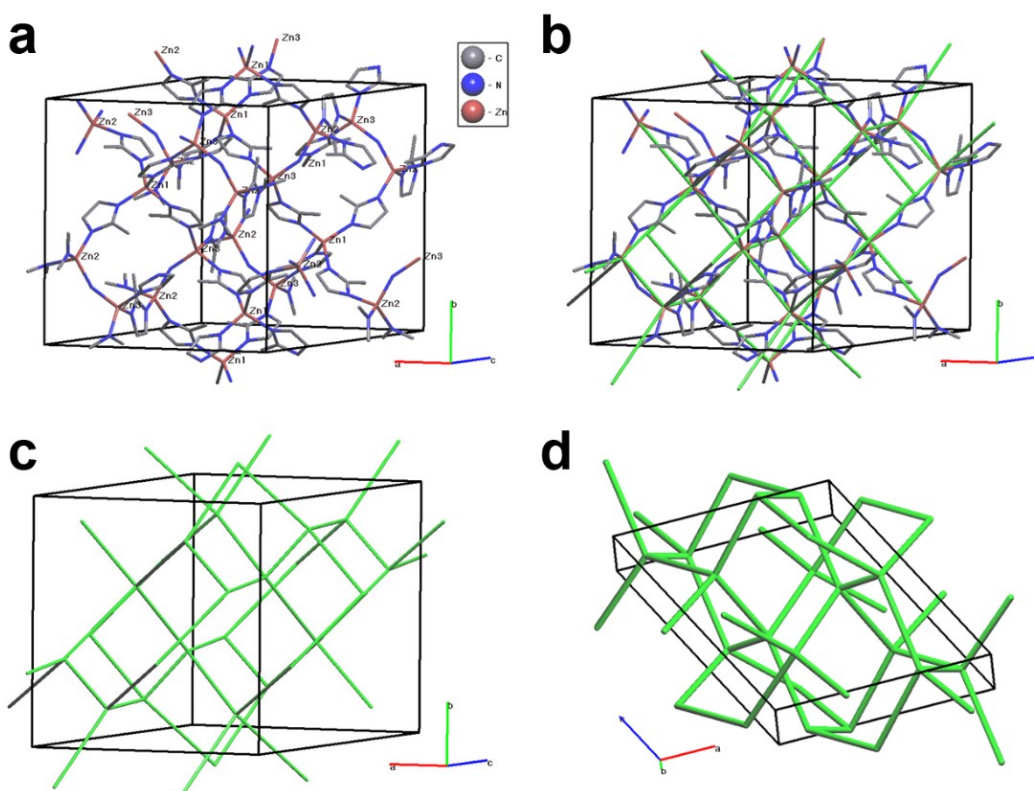


Figure S5. (a) The structural model of ZIF-EC1. (b-d) The definition of the underlying net, which is shown in green. Each of the three independent Zn are 4-c nodes and each ligand is bridging two Zn atoms. From the coordinates of the underlying net, ToposPro find that it is a known binodal net (meaning that two of the three Zn atoms are topologically equivalent) called *yqt1*. It is defined as a 4,4-c net with stoichiometry (4-c)(4-c)₂, and a 2-nodal net with the point symbol of (5.6².7².8)(5².6.7.8²)₂, and the vertex symbol of [5.8₄.5.8₅.6.8₅] [5.8₅.6.6.8₄.8₄].

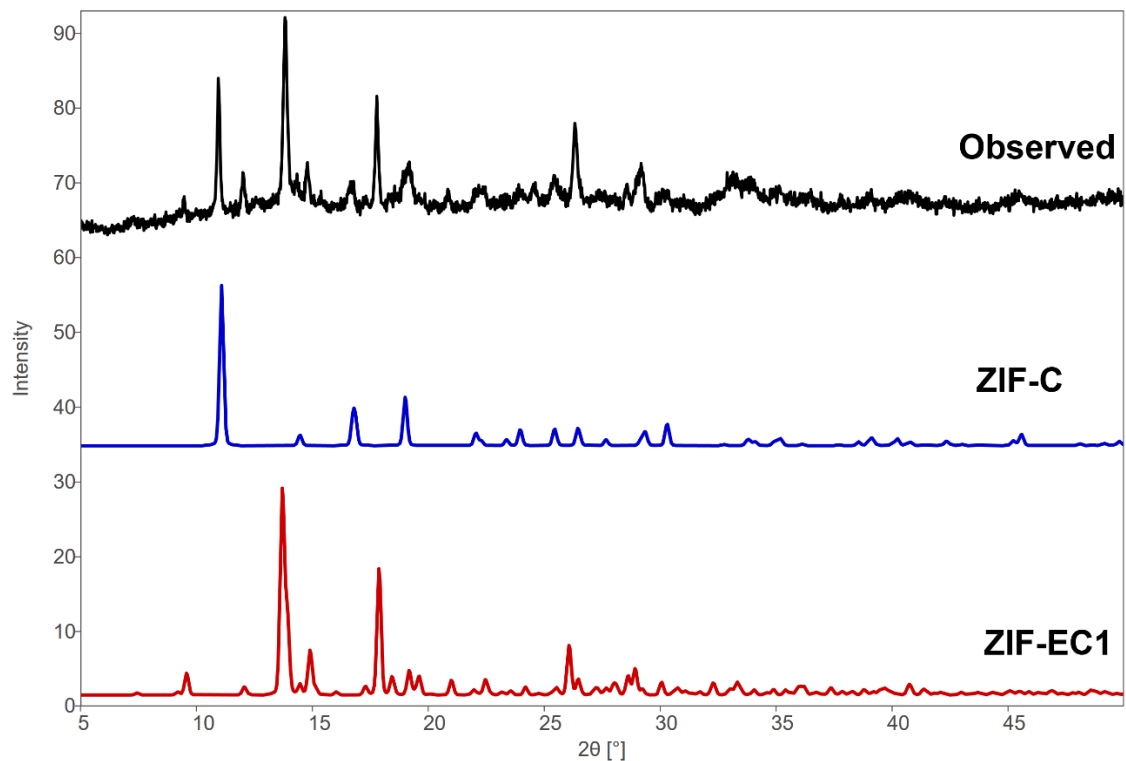


Figure S6. Comparison of the observed PXRD pattern of the phase mixture with the simulated PXRD patterns of ZIF-CO₃-1 and ZIF-EC1. All peaks in the observed pattern can be indexed using the two phases. The PXRD patterns were simulated from the corresponding structural models using a pseudo-Voigt peak shape function.

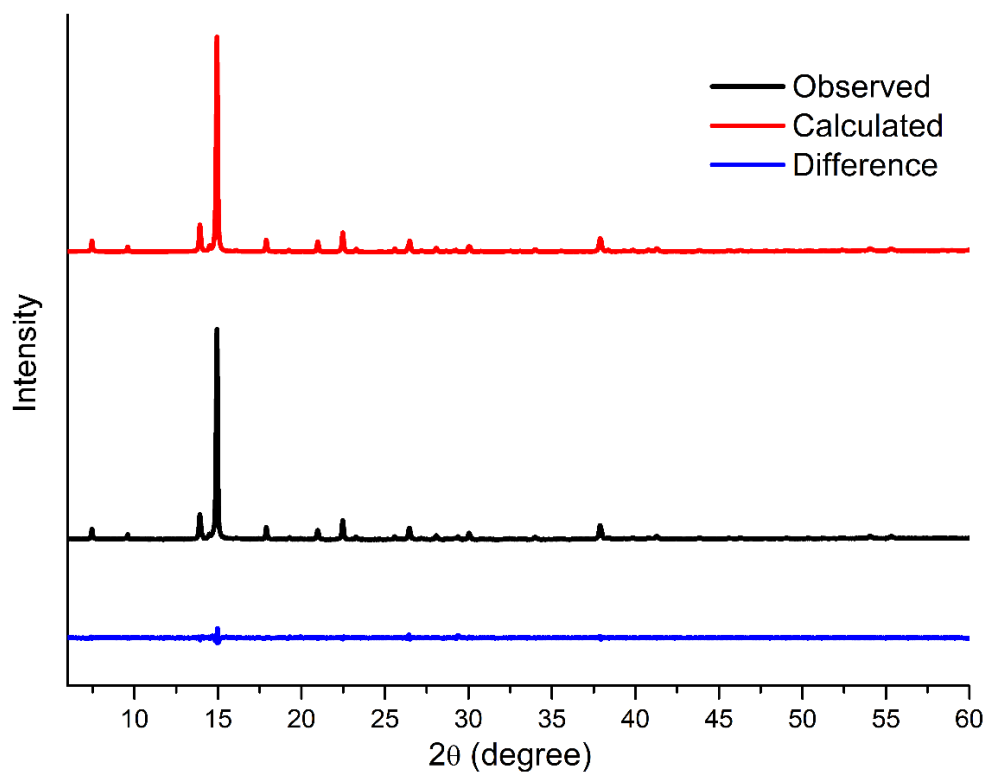


Figure S7. Pawley fit of the experimental PXRD pattern ($\lambda = 1.5406 \text{ \AA}$) of ZIF-EC1, which shows a good agreement indicating the sample is pure ZIF-EC1.

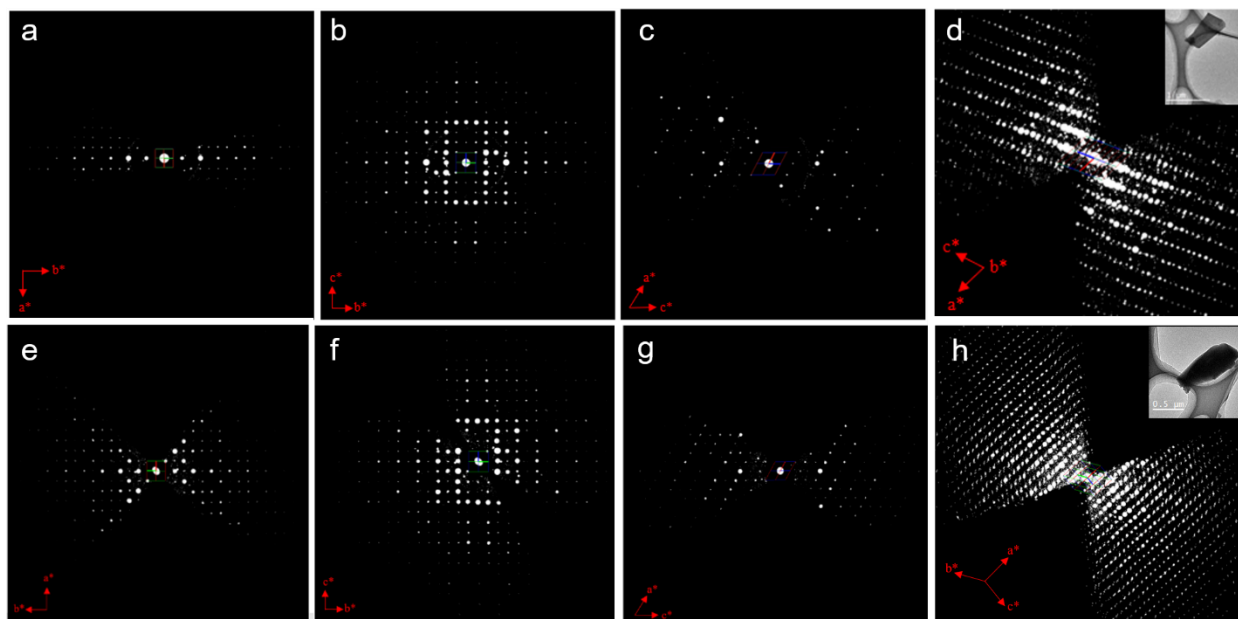


Figure S8. Reciprocal lattices reconstructed from cRED data. (a-d) 2D slice cuts of (a) $hk0$, (b) $0kl$, and (c) $h0l$ planes from the reconstructed 3D reciprocal lattice (d) of a ZIF-EC1 crystal (inset in d) in the phase mixture. (e-h) 2D slice cuts of (e) $hk0$, (f) $0kl$, and (g) $h0l$ planes from the reconstructed 3D reciprocal lattice (h) of a ZIF-EC1 crystal (inset in h) in the pure ZIF-EC1 sample.

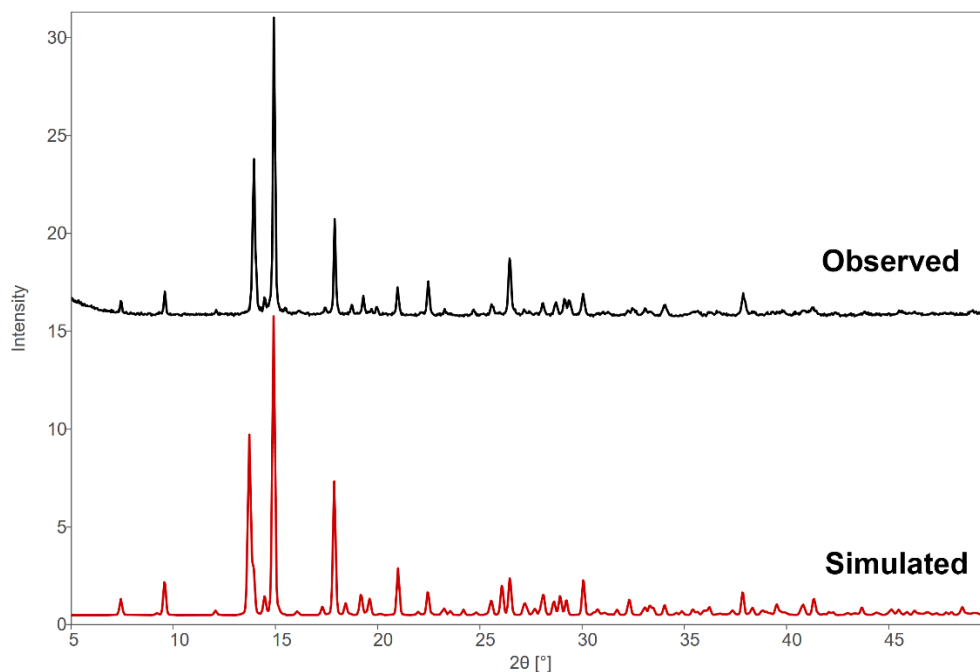


Figure S9. Comparison of observed and simulated PXRD patterns of ZIF-EC1 ($\lambda = 1.5406 \text{ \AA}$). The PXRD pattern were simulated using a pseudo-Voigt peak shape function, with the preferred orientation simulated using a weighted March-type correction.

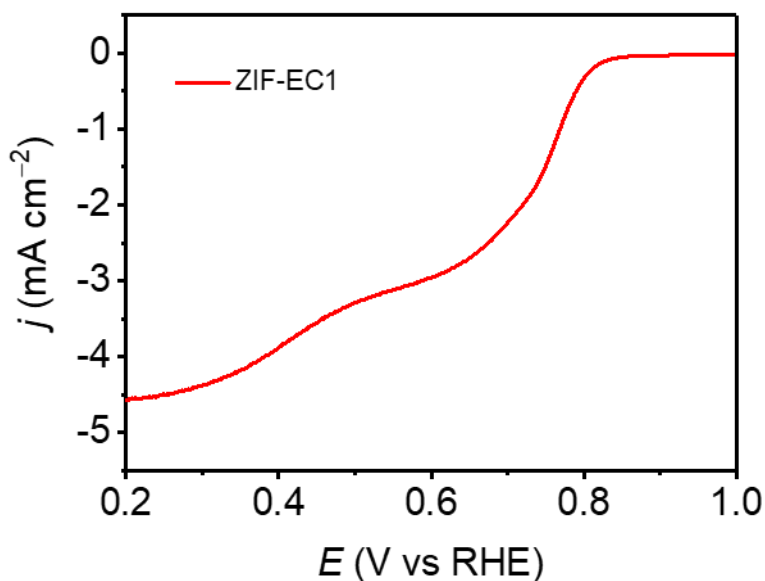


Figure S10. LSV curves of ZIF-EC1 in 0.1 M KOH solution saturated by O_2 . The ZIF-EC1 sample was mixed with 50% carbon black. The $E_{1/2}$ of ZIF-EC1 was measured to be 0.757 V, indicating a moderate ORR activity.

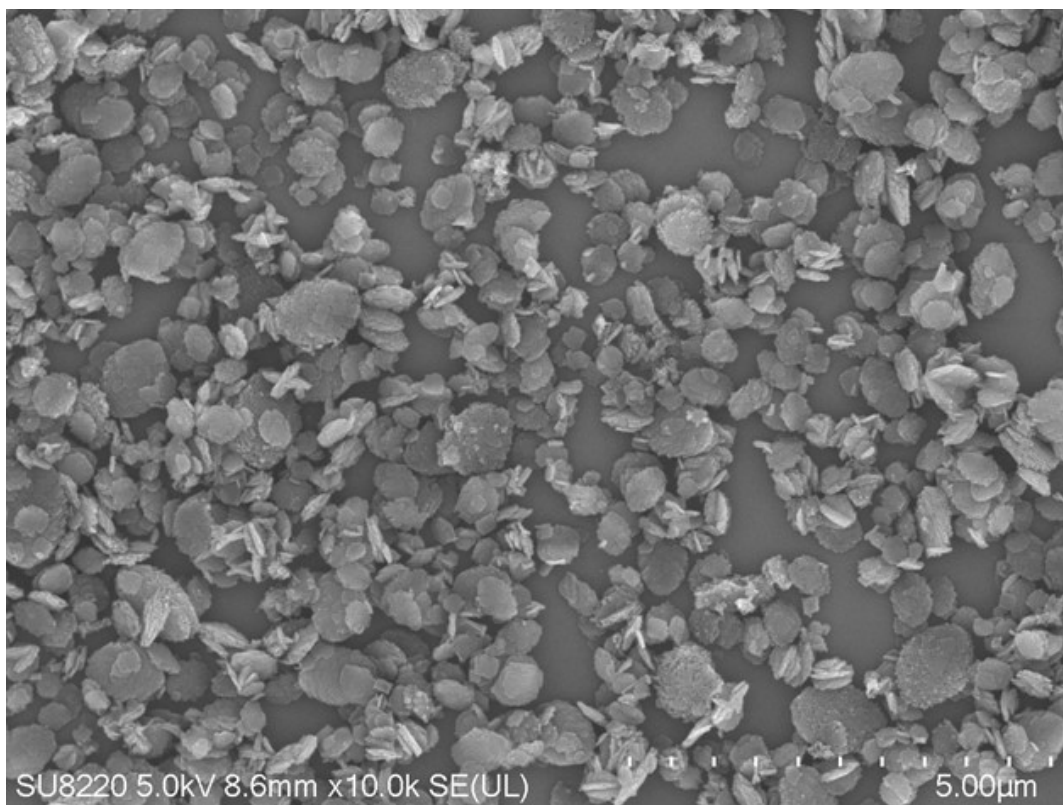


Figure S11. SEM image of NC-ZIF-EC1 nanocrystals.

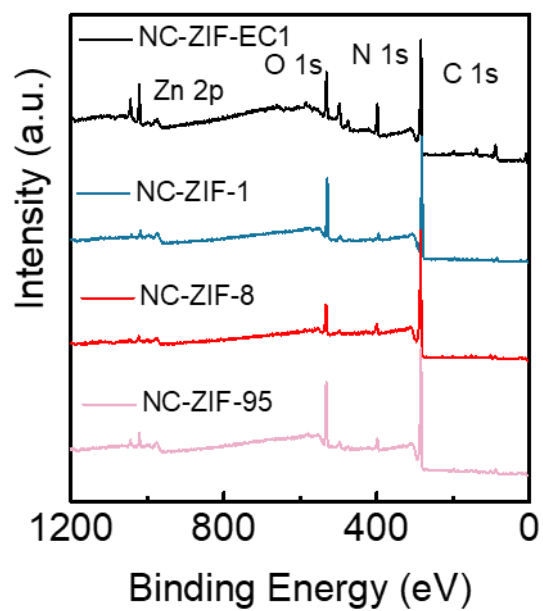


Figure S12. XPS spectra of NC-ZIF-EC1, NC-ZIF-1, NC-ZIF-8, and NC-ZIF-95. The contents of C, N, O, Zn calculated based on XPS are summarized in Table S4.

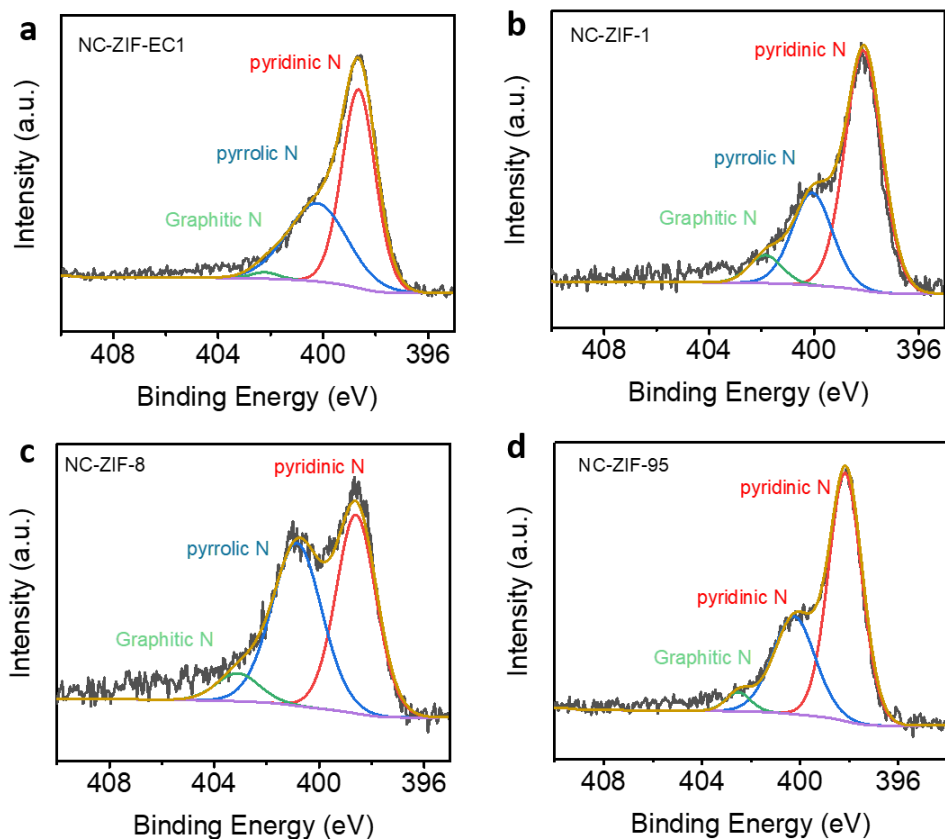


Figure S13. High-resolution XPS spectra of N 1s for NC-ZIF-EC1 (a), NC-ZIF-1 (b), NC-ZIF-8 (c), and NC-ZIF-95 (d).

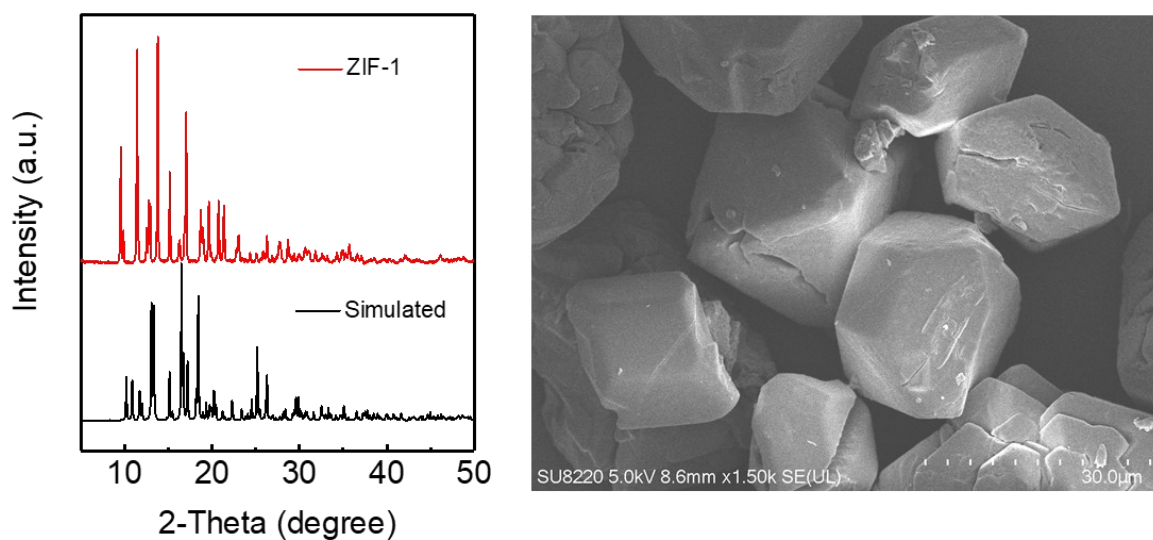


Figure S14. PXRD pattern (left) and SEM image (right) of ZIF-1.

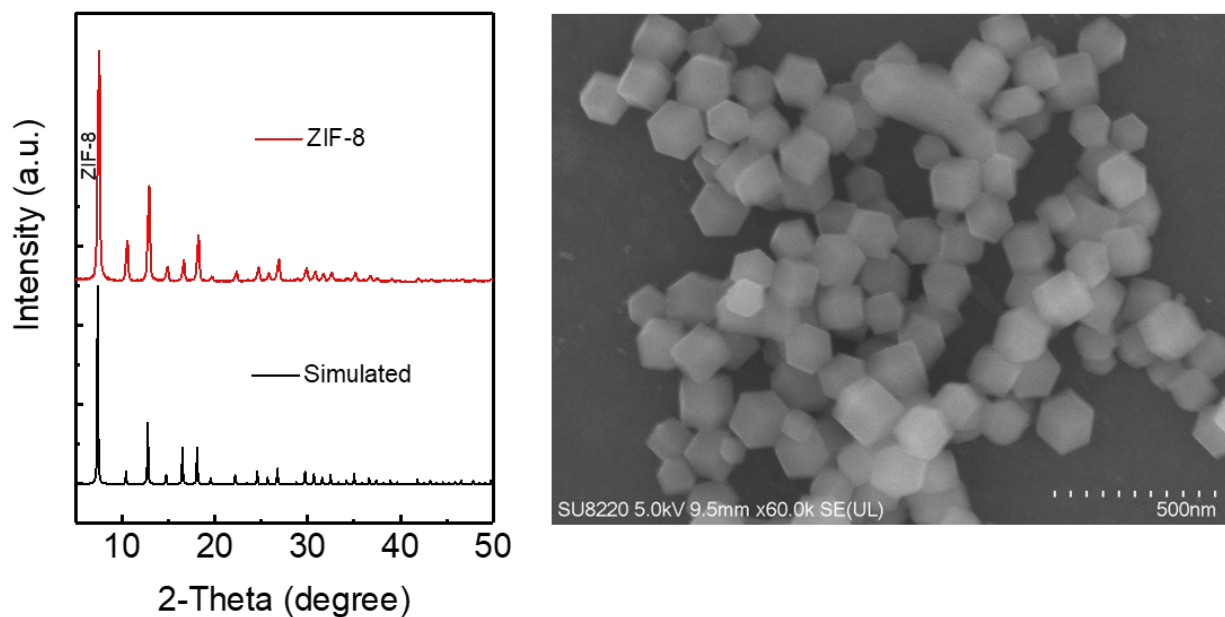


Figure S15. PXR D pattern (left) and SEM image (right) of ZIF-8.

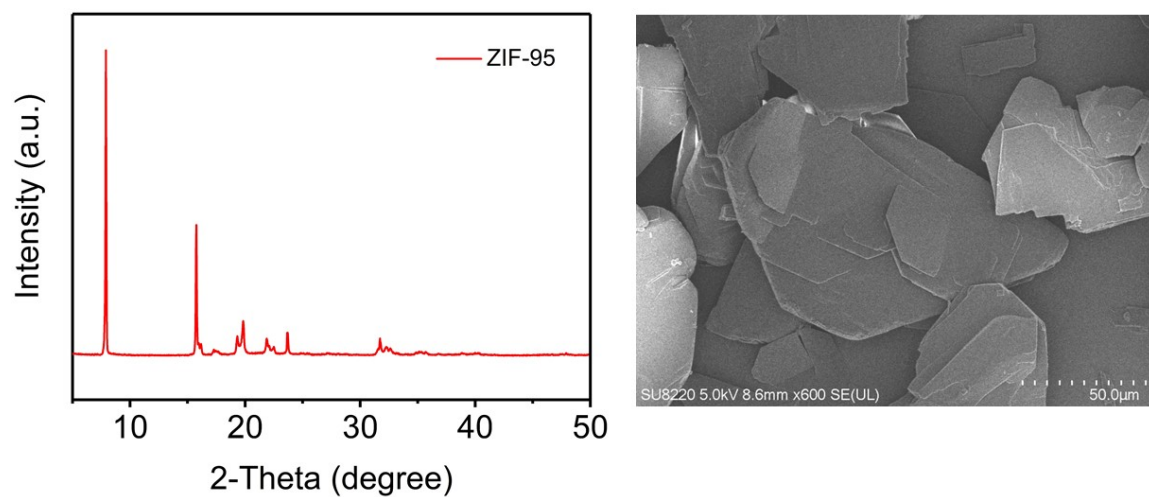


Figure S16. PXR D pattern (left) and SEM image (right) of ZIF-95.

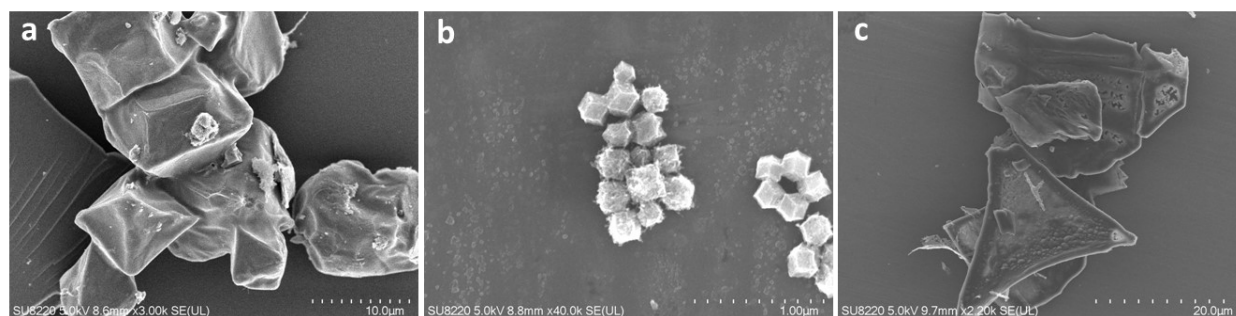


Figure S17. SEM images of (a) NC-ZIF-1, (b) NC-ZIF-8, and (c) NC-ZIF-95.

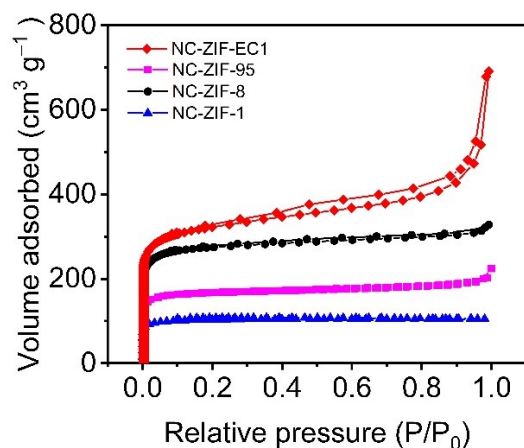


Figure S18. N₂ adsorption-desorption isotherm of NC-ZIF-EC1, NC-ZIF-1, NC-ZIF-8, and NC-ZIF-95, from which the Brunauer-Emmett-Teller (BET) surface areas are estimated as 1226, 1079, 657, and 295 m²g⁻¹, respectively.

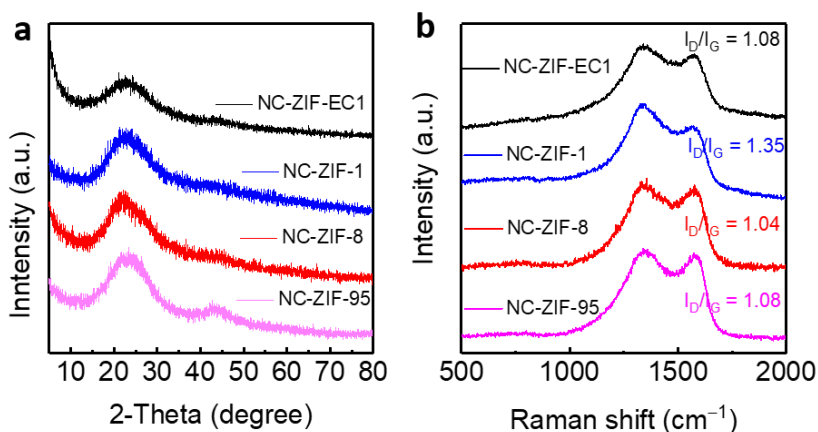


Figure S19. PXRD patterns (a) and Raman spectra (b) of various N doped carbon materials derived from different ZIFs.

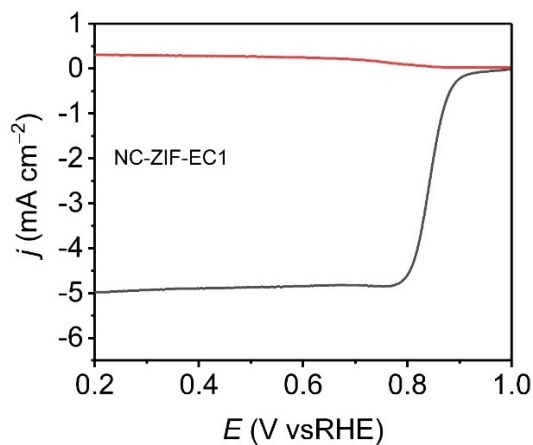


Figure S20. LSV curves of the NC-ZIF-EC1 in O₂-saturated 0.1 M KOH solution using a rotating ring disk electrode with a scan rate of 5 mV s⁻¹ and a rotation speed of 1600 rpm.

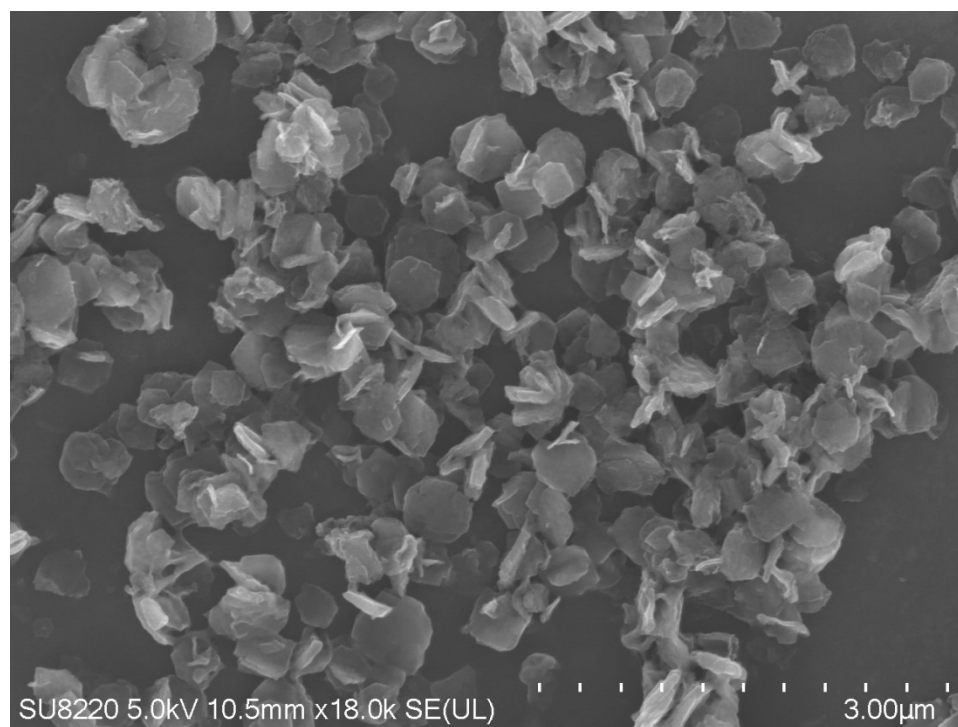


Figure S21. SEM image of NC-ZIF-EC1 after ORR reaction.

Table S1. Details of cRED data collection on different nanocrystals in the phase mixture, and the corresponding unit cell parameters and space groups deduced from the cRED data.

Dataset	1	2	3	4	5	6	7	8	9	10	11
Phase	ZIF-CO ₃ -1									ZIF-EC1	
Rotation range (°)	100.18	103.57	93.91	60.31	74.01	54.06	48.35	43.60	39.26	117.45	42.34
Rotation step (°)	0.9	0.9	0.9	0.9	0.9	0.9	0.9	0.9	0.9	1.5	0.9
Exposure time (s frame ⁻¹)	0.5	0.5	0.5	0.5	0.5	0.5	0.5	0.5	0.5	0.3	0.5
No. of frames	390	402	365	238	287	208	187	170	153	748	165
Total data collection time (min)	3.7	3.8	3.5	2.3	2.7	2.0	1.8	1.6	1.5	4.3	1.6
Crystal system	Orthorhombic									Monoclinic	
Space group	<i>Pba2</i> (No. 32) or <i>Pbam</i> (No. 55)									<i>P2₁/c</i>	
<i>a</i> (Å)	10.501	10.500	10.547	10.474	10.513	10.89	10.94	10.84	10.81	13.579	14.035
<i>b</i> (Å)	12.507	12.400	12.236	12.162	12.331	12.84	12.63	12.52	12.93	14.550	15.379
<i>c</i> (Å)	4.691	4.600	4.669	4.548	4.664	4.88	4.77	4.68	4.87	14.314	14.620
α (°)	90	90	90	90	90	90	90	90	90	90.000	90.000
β (°)	90	90	90	90	90	90	90	90	90	117.98	118.419
γ (°)	90	90	90	90	90	90	90	90	90	90.000	90.000

Table S2. Crystallographic data and refinement details of ZIF-EC1.

	Phase mixture	Pure phase*
Wavelength (Å)	0.02508 Å	0.02508 Å
Resolution (Å)	0.90	0.78
Crystal system	Monoclinic	Monoclinic
Space group	<i>P</i> 2 ₁ / <i>c</i> (No. 14)	<i>P</i> 2 ₁ / <i>c</i> (No. 14)
<i>a</i> (Å)	13.579(3)	13.462(2)
<i>b</i> (Å)	14.550(3)	14.659(3)
<i>c</i> (Å)	14.314(3)	14.449(2)
β (°)	117.98(3)	118.12(1)
Volume (Å ³)	2497.5(11)	2514.7(8)
Completeness (%)	61.4	89.5
No. unique reflections	2008	5116
No. observed reflections (<i>I</i> > 2 sigma(<i>I</i>))	878	4103
<i>R</i> ₁ (<i>I</i> > 2 sigma(<i>I</i>))	0.238	0.181
<i>R</i> ₁ (all reflections)	0.301	0.198
Goof	1.314	1.725

* Nine datasets are merged.

Table S3. Crystallographic data and Pawley fitting results of ZIF-EC1.

Chemical formula	C ₂₀ N ₁₀ OZn ₃
Formula weight	592.47
Crystal system	Monoclinic
Space group	<i>P</i> 2 ₁ / <i>c</i> (No. 14)
<i>a</i> /Å	13.461(2)
<i>b</i> /Å	14.659(3)
<i>c</i> /Å	14.449(2)
β /°	118.12(2)
Temperature/K	298(2)
Wavelength/Å	1.54056
2 θ range/°	5.998356 – 59.990356
R _p	0.0471
R _{wp}	0.0667
R _{exp}	0.0429
GOOF	1.552

Table S4. Elemental contents (wt%) in different catalysts estimated by XPS.

Catalyst	C	N	O	Zn
NC-ZIF-EC1	69.49±0.016	13.41±0.02	12.95±0.03	2.12±0.71
NC-ZIF-1	77.02±0.021	4.05±0.011	17.11±0.092	0.49±0.077
NC-ZIF-8	80.74±0.013	6.52±0.054	10.02±0.081	0.32±0.12
NC-ZIF-95	75.23±0.034	6.42±0.143	16.46±0.094	0.71±0.044

Table S5. Comparison of the onset potential E_{onset} and half-wave potential $E_{1/2}$ of NC materials for ORR.

Catalyst	E_{onset} vs RHE (V)	$E_{1/2}$ vs RHE (V)
NC-ZIF-EC1	0.930	0.860
NC-ZIF-1	0.880	0.807
NC-ZIF-8	0.910	0.836
NC-ZIF-95	0.855	0.720
Pt/C	0.940	0.867

Table S6. Comparison of the performance of NC-ZIF-EC1 with previously reported electrocatalysts.

Catalyst	Electrolyte	$E_{1/2}$ (vs RHE)	Ref.
NC-ZIF-EC1	0.1 M KOH	0.860 V	This work
Zn-N-C	0.1 M KOH	0.850 V	[8]
ZnN _x /BP	0.1 M KOH	0.837 V	[9]
Zn-NC-1	0.1 M KOH	0.873 V	[10]
CoZn-NC-700	0.1 M KOH	0.840 V	[11]
CoFeZn/NC	0.1 M KOH	0.850 V	[12]
M (M = Co and Zn) ₂ P ₂ O ₇ @NC	0.1 M KOH	0.793 V	[13]
ZCP-CFs-9 (Zn, Co-ZIF)	0.1 M KOH	0.829 V	[14]
Ni ₃ (HITP) ₂	0.1 M KOH	0.82 V	[15]
Fe-TAPP COF aerogel	0.1 M KOH	0.83 V	[16]
2D CAN-Pc(Fe/Co)	0.1 M KOH	0.84 V	[17]
PcCu-O ₈ -Co MOF	0.1 M KOH	0.83 V	[18]
NCo@CNT-NF700	0.1 M KOH	0.87 V	[19]
MnO/Co/PGC	0.1 M KOH	0.78 V	[20]
Co ₂ VO ₄	1.0 M KOH	0.83 V	[21]

NC=Nitrogen doped carbon; BP=carbon black; CF=carbon fibers; HITP=hexaiminotriphenylene; TAPP=5,10,15,20-(Tetra-4-aminophenyl)porphyrin; CAN=conjugated aromatic networks; Pc=phthalocyanine; CNT=carbon nanotube; NF=nanofiber; PGC=porous graphitic carbon

References

- [1] M. O. Cichocka, J. Ångström, B. Wang, X. Zou, S. Smeets, *J. Appl. Crystallogr.* **2018**, *51*, 1652–1661.
- [2] W. Wan, J. Sun, J. Su, S. Hovmöller, X. Zou, *J. Appl. Crystallogr.* **2013**, *46*, 1863–1873.
- [3] W. Kabsch, *Acta Crystallogr. D Biol. Crystallogr.* **2010**, *66*, 133–144.
- [4] S. R. Bahn, K. W. Jacobsen, *Comput. Sci. Eng.* **2002**, *4*, 56–66.
- [5] P. Giannozzi, S. Baroni, N. Bonini, M. Calandra, R. Car, C. Cavazzoni, D. Ceresoli, G. L. Chiarotti, M. Cococcioni, I. Dabo, A. D. Corso, S. de Gironcoli, S. Fabris, G. Fratesi, R. Gebauer, U. Gerstmann, C.

- Gougoussis, A. Kokalj, M. Lazzeri, L. Martin-Samos, N. Marzari, F. Mauri, R. Mazzarello, S. Paolini, A. Pasquarello, L. Paulatto, C. Sbraccia, S. Scandolo, G. Sclauzero, A. P. Seitsonen, A. Smogunov, P. Umari, R. M. Wentzcovitch, *J. Phys. Condens. Matter* **2009**, *21*, 395502.
- [6] A. A. Adllan, A. D. Corso, *J. Phys. Condens. Matter* **2011**, *23*, 425501.
- [7] S. Grimme, J. Antony, S. Ehrlich, H. Krieg, *J. Chem. Phys.* **2010**, *132*, 154104.
- [8] J. Wang, H. Li, S. Liu, Y. Hu, J. Zhang, M. Xia, Y. Hou, J. Tse, J. Zhang, Y. Zhao, *Angew. Chem. Int. Ed.* DOI: 10.1002/anie.202009991.
- [9] P. Song, M. Luo, X. Liu, W. Xing, W. Xu, Z. Jiang, L. Gu, *Adv. Funct. Mater.* **2017**, *27*, 1700802.
- [10] J. Li, S. Chen, N. Yang, M. Deng, S. Ibraheem, J. Deng, J. Li, L. Li, Z. Wei, *Angew. Chem. Int. Ed.* **2019**, *58*, 7035–7039.
- [11] B. Chen, X. He, F. Yin, H. Wang, D.-J. Liu, R. Shi, J. Chen, H. Yin, *Adv. Funct. Mater.* **2017**, *27*, 1700795.
- [12] J. Wang, W. Zang, S. Xi, M. Kosari, S. J. Pennycook, H. Chun Zeng, *J. Mater. Chem. A* **2020**, *8*, 17266–17275.
- [13] L.-H. Xu, H.-B. Zeng, X.-J. Zhang, S. Cosnier, R. S. Marks, D. Shan, *J. Catal.* **2019**, *377*, 20–27.
- [14] C. Liu, J. Wang, J. Li, J. Liu, C. Wang, X. Sun, J. Shen, W. Han, L. Wang, *J. Mater. Chem. A* **2017**, *5*, 1211–1220.
- [15] E. M. Miner, T. Fukushima, D. Sheberla, L. Sun, Y. Surendranath, M. Dincă, *Nat. Commun.* **2016**, *7*, 10942.
- [16] N. Zion, D. A. Cullen, P. Zelenay, L. Elbaz, *Angew. Chem. Int. Ed.* **2020**, *59*, 2483–2489.
- [17] S. Yang, Y. Yu, M. Dou, Z. Zhang, L. Dai, F. Wang, *Angew. Chem. Int. Ed.* **2019**, *58*, 14724–14730.
- [18] H. Zhong, K. H. Ly, M. Wang, Y. Krupskaya, X. Han, J. Zhang, J. Zhang, V. Kataev, B. Büchner, I. M. Weidinger, S. Kaskel, P. Liu, M. Chen, R. Dong, X. Feng, *Angew. Chem. Int. Ed.* **2019**, *58*, 10677–10682.
- [19] L. Zou, C.-C. Hou, Z. Liu, H. Pang, Q. Xu, *J. Am. Chem. Soc.* **2018**, *140*, 15393–15401.
- [20] X. F. Lu, Y. Chen, S. Wang, S. Gao, X. W. (David) Lou, *Adv. Mater.* **2019**, *31*, 1902339.
- [21] C. Mu, J. Mao, J. Guo, Q. Guo, Z. Li, W. Qin, Z. Hu, K. Davey, T. Ling, S.-Z. Qiao, *Adv. Mater.* **2020**, *32*, 1907168.